Convective Initiation at the Dryline: A Modeling Study

CONRAD L. ZIEGLER

NOAA/National Severe Storms Laboratory, Norman, Oklahoma

TSENGDAR J. LEE* AND ROGER A. PIELKE SR.

Department of Atmospheric Science, Colorado State University, Fort Collins, Colorado

(Manuscript received 25 April 1996, in final form 24 September 1996)

ABSTRACT

A nonhydrostatic, three-dimensional version of the Colorado State University Regional Atmospheric Modeling System (CSU-RAMS) is used to deduce the processes responsible for the formation of drylines and the subsequent initiation of deep, moist dryline convection. A range of cumuliform cloud types are explicitly simulated along drylines on 15, 16, and 26 May 1991 in accordance with observations.

In the simulations, narrow convergence bands along the dryline provide the lift to initiate deep moist convection. The thermally direct secondary convective boundary layer (CBL) circulations along the dryline are frontogenetic and solenoidally forced. Maximum updrafts reach 5 m s^{-1} and the bands are 3–9 km wide and 10–100 km or more in length. The updrafts penetrate and are decelerated by the overlying stable air above the CBL, reaching depths of about 2000 m in the cases studied. Moisture convergence along the mesoscale updraft bands destabilizes the local sounding to deep convection, while simultaneously decreasing the CIN to zero where storms subsequently develop. The lapse rates of vapor mixing ratio and potential temperature in the mesoscale updrafts are rather small, indicating that increases of the lifted condensation level (LCL) and level of free convection (LFC) due to mixing following the parcel motion are also small. Simulated convective clouds of all modes, including shallow forced cumulus and storms, develop in regions where the CIN ranges from zero up to the order of the peak kinetic energy of the boundary layer updraft and moisture is sufficiently deep to permit water saturation to develop in the boundary layer.

The findings suggest that classic cloud models may not adequately simulate the early development of dryline storms due to their use of thermal bubbles to initiate convection and their assumption of a horizontally homogeneous environment. In contrast, cautious optimism may be warranted in regard to operational numerical prediction of drylines and the threat of attendant deep convection with mesoscale models.

1. Introduction

Recent interest in studying the dryline of the southern Plains is motivated by the frequency of thunderstorm formation there during the spring and early summer months (Rhea 1966). A mesoscale boundary separating warm, moist air from the Gulf of Mexico and hot, dry air from the elevated terrain of northern Mexico and the southwest United States (Schaefer 1986), the dryline is often the focus of severe weather. Of particular interest are the location, mode, morphology, and organization of deep dryline convection (Koch and McCarthy 1982; Bluestein and Parker 1993) and the timing of convective initiation. Though the topic of convective interaction and organization is beyond the scope of the present study, an excellent review on this subject may be found in Cotton and Anthes (1989). In spite of the apparent role of the dryline to initiate and organize deep convection, cumulus cloud lines often form there without evolving into storms on some days with strong localized convergence, abundant moisture, and weak stability to convective motions in the boundary layer.

Adopting the definition of ''mesoscale'' proposed by Orlanski (1975), both the dryline and individual deep convective clouds are typically meso-γ scale in width (2–20 km), while the dryline environment may be characterized as meso-β scale in width (20–200 km). The dryline typically ranges from 500 to 1000 km in length. Since storms often form within 10–20 km of the dryline, boundary layer variability at these meso-γ scales is probably critical for the storm initiation process. The fields of convective inhibition (CIN), convective available potential energy (CAPE), and vertical wind shear cannot be adequately resolved with conventional surface or upper-air operational observing systems at the meso-

*Current affiliation: Planning Research Corporation, McLean, Virginia.

Corresponding author address: Dr. Conrad L. Ziegler, National Severe Storms Laboratory, Mesoscale Research and Applications Division, 1313 Halley Circle, Norman, OK 73069.
E-mail: ziegler@nssl.uoknor.edu

γ scale typifying the strongest cross-dryline gradients (Parsons et al. 1991; Ziegler and Hane 1993; Hane et al. 1993; Ziegler et al. 1995). Due to the lack of mesoscale observational resolution, the operational mesoanalysis of the dryline is difficult (Doswell 1982). Due to the combination of limited observational resolution with a poor understanding of the convective initiation process itself, forecasting the initiation and subsequent mode of dryline convection is a challenging problem (Doswell 1987; Johns and Doswell 1992; McNulty 1995).

Although at present there is poor understanding of the conditions in the immediate vicinity of the dryline on the meso-γ scales of isolated storms, we have a relatively good understanding of the morphology of the meso-β-scale dryline environment and its role in controlling the likelihood that dryline storms will develop. Following an ''ingredients-based'' forecasting approach, the joint occurrence of small values of CIN, high CAPE values, and deep tropospheric wind shear along a well-defined mesoscale boundary with strong low-level convergence suggests a high likelihood for severe storms *given the initiation of convection* (Johns and Doswell 1992; McNulty 1995). Even if CAPE and wind shear are at marginal levels to support severe convection, conditions may nevertheless be sufficient for the development of nonprecipitating convective clouds or nonsevere storms at the dryline. Although the increase of static energy and some lifting destabilization occur on meso-β or larger scales, it is now widely accepted by forecasters and researchers that the release of the instability is focused by organized meso-γ scale boundary layer lift. Both the relative intensities of the capping inversion above the convective boundary layer (CBL), proportional to the magnitude of the CIN, and the mesoscale lift are believed to be critical to the potential for deep convection to develop. Prior to the present study, the coincident levels of mesoscale lifting and CIN needed to initiate dryline convection have not been quantified.

Differential heating and solenoidally driven upslope flow in the dryline environment generate boundary layer convergence, which increases horizontal contrasts of temperature and water vapor by frontogenesis (e.g., Sun and Ogura 1979; Anthes et al. 1982; Benjamin 1986; Benjamin and Carlson 1986; Sun and Wu 1992; Ziegler et al. 1995). Differential heating is enhanced by inhomogeneities of soil moisture and vegetation (e.g., Benjamin 1986; Benjamin and Carlson 1986; Lanicci et al. 1987; Lakhtakia and Warner 1987; Chang and Wetzel 1991; Sun and Wu 1992; Ziegler et al. 1995). Several mechanisms have been proposed for concentrating and releasing potential buoyant energy leading to the initiation of convective storms. Colby (1984), Pielke and Zeng (1989), Segal et al. (1995), and Clark and Arritt (1995) have argued that surface heating and evaporation of ground moisture with subsequent vertical turbulent transport promote the injection of moist static energy into the CBL, resulting in a lowering of the lifted condensation level (LCL) and the level of free convection (LFC) and deepening of the CBL with an accompanying decrease of CIN. The reduction of CIN may occur either by progressive weakening of the capping inversion during growth of the CBL, by regional-scale lifting or following the motion of boundary layer air as it moves out from under the capping inversion (Carlson and Ludlam 1968; Carlson et al. 1983; Keyser and Carlson 1984; Graziano and Carlson 1987; Lanicci and Warner 1991).

Relatively few studies have discussed properties of the boundary layer nearby or beneath convective clouds in their earliest developing stage, due to the difficulties of collecting representative in situ measurements on the scales of individual clouds that have not yet formed. Special mesoscale observations collected by a variety of mobile instrumented platforms and ground-based Doppler radars have provided important insights regarding the environments of developing convection. NSSP Staff (1963) present aircraft observations of temporally coherent, upward-bulging moist, cool tongues of air, essentially parallel to the dryline, near where cumulus clouds occasionally develop, and suggest that these moist bulges may be causally linked to the initiation of thunderstorms. Wilson et al. (1988) document the presence of strong secondary circulations that apparently deepen the boundary layer along a stationary, terrain-induced convergence line where storms subsequently develop. Hane et al. (1993) show examples of moisture bulges along drylines, suggesting that the moist plumes are feeding active cumulus congestus observed above the aircraft during the stepped traverse patterns. Wakimoto and Atkins (1994) and Atkins et al. (1995) use dual-Doppler radar and aircraft observations to document the initiation of cumulus near the intersection points of the sea-breeze front with horizontal convective roll (HCR) circulations formed within the CBL ahead of the advancing sea-breeze front. In another sea-breeze study, Fankhauser et al. (1995) document the initiation of deep convection from the interactions of these HCRs with an outflow boundary from preexisting storms. Banta (1984), Banta and Schaaf (1987), and Schaaf et al. (1988) have shown how convergence lines in the lee of mountain ranges may provide sufficient localized moisture uplift to initiate cumulus clouds and thunderstorms. Stull (1985) categorizes boundary layer cumulus clouds according to whether the needed lifting to achieve water saturation is forced by boundary layer thermals exclusively (i.e., forced convection) or alternatively enhanced by the release of buoyant cloud energy and the resulting vertical acceleration of subcloud air by pressure forces (i.e., active convection).

In the present study we use a mesoscale model to infer the triggering processes of deep, moist convection in several cases where dryline storms and their mesoscale environment have been observed. Recent improvements of mesoscale models now provide the ability to represent not only the evolution of the parent mesoscale

TABLE 1. Configuration of optional physics, numerics, and initialization schemes of the Colorado State University (CSU) mesoscale model for the dryline study.

Category	Option(s) used
Basic equations	3D; nonhydrostatic; compressible
Vertical coordinate	Terrain-following σ_z
Horizontal coordinate	Stereographic tangent plane
Grid stagger and structure	Arakawa C grid; multiple, fixed nested grids
Time differencing	Leapfrog; time split; second- or fourth-order spatial accuracy
Turbulence closure	*K* from deformation (Smagorinsky), scaled up or down by Ri
Microphysics	• Warm microphysics on cloud-resolving fine nested grid • Condensation only (i.e., no microphysics) on coarse grids
Cumulus parameterization	None
Radiation	Effects of clouds and water vapor
Surface layer	Parametric flux model with bulk Ri dependence
Lower boundary	• Prognostic soil model for moisture and temperature • Vegetation parameterization
Upper boundary	Rigid lid with modified Rayleigh absorbing layer
Lateral boundaries	• Klemp and Wilhelmson (1978) • Nudging from regional scale conditions (outer grid)
Initialization	• 3D isentropic objective analysis of NMC Nested Grid Model output and NWS radiosonde data • 2D objective analysis of surface data • Isentropic and surface analyses interpolated to RAMS grid

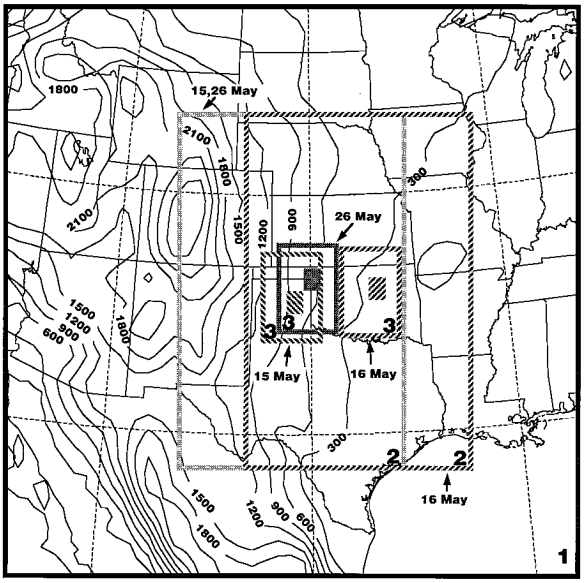

FIG. 1. The location of three nested grids within the outer grid for the simulations on 15, 16, and 26 May 1991. The contours are terrain on grid 1 (m MSL), generated by interpolating from a dataset with 10′ spacing to the 60-km mesh. Small filled rectangles denote the locations of grid 4 for each case, and fill type is the same as the line fill used for grid 3 on a given day.

circulations and storm environments but also the convective storms themselves within the same simulation. Thus, a continuum of atmospheric weather phenomena ranging from the meso-α or synoptic scale down through the meso-γ scale are represented. The present approach therefore complements, and yet is distinct from, classic storm simulation methods (e.g., Klemp and Wilhelmson 1978). In what follows, we describe our modeling approach and aspects of our simulations of the drylines of 15, 16, and 26 May 1991, which have been described by Hane et al. (1993). We focus attention on the relationship of the initial convection to the moisture field, the stability to convective motions (i.e., CIN), and the airflow circulations in the boundary layer, while also demonstrating the capability of simulating realistic deep convection within the mesoscale model framework. Section 2 describes the mesoscale model and the initialization method, while section 3 presents the results of the simulations. A discussion of the results in section 4 is followed by concluding remarks in section 5.

2. Mesoscale model

To explicitly resolve deep, moist convection along the dryline, we have employed the three-dimensional, nonhydrostatic version of the Colorado State University Regional Atmospheric Modeling System (CSU-RAMS). From a suite of optional physics modules, grid configurations, and numerical schemes described in Pielke et al. (1992), the model is configured for the present study as listed in Table 1. Running the three-dimensional version also allows us to confirm and extend results of dryline simulations made with a 2D version of RAMS reported by Ziegler et al. (1995). The model includes full primitive equations for the *u*, *v*, and *w* components of momentum. The model domain is characterized by a terrain-following vertical coordinate and Cartesian horizontal coordinates on a series of nested grids. Turbulence is parameterized with a first-order or *K*-theory closure with a local, deformation-based turbulent exchange coefficient that is dependent on the local value of the Richardson number (Ri). A multilevel prognostic soil model is fully coupled with a vegetation model (Avissar and Mahrer 1988) to calculate temperature and moisture variations in the soil, as well as sensible and latent heat fluxes through the atmospheric surface layer.

a. Grid configuration and terrain

A total of four fixed grids are employed (Fig. 1), the inner three being two-way interactive nested grids. The fine grid is intended to explicitly resolve deep moist convection, while the coarser meshes resolve the dryline and the synoptic environment. The vacillations of the drylines are followed by centering the inner two grids over the eastern Texas panhandle for the 15 May case,

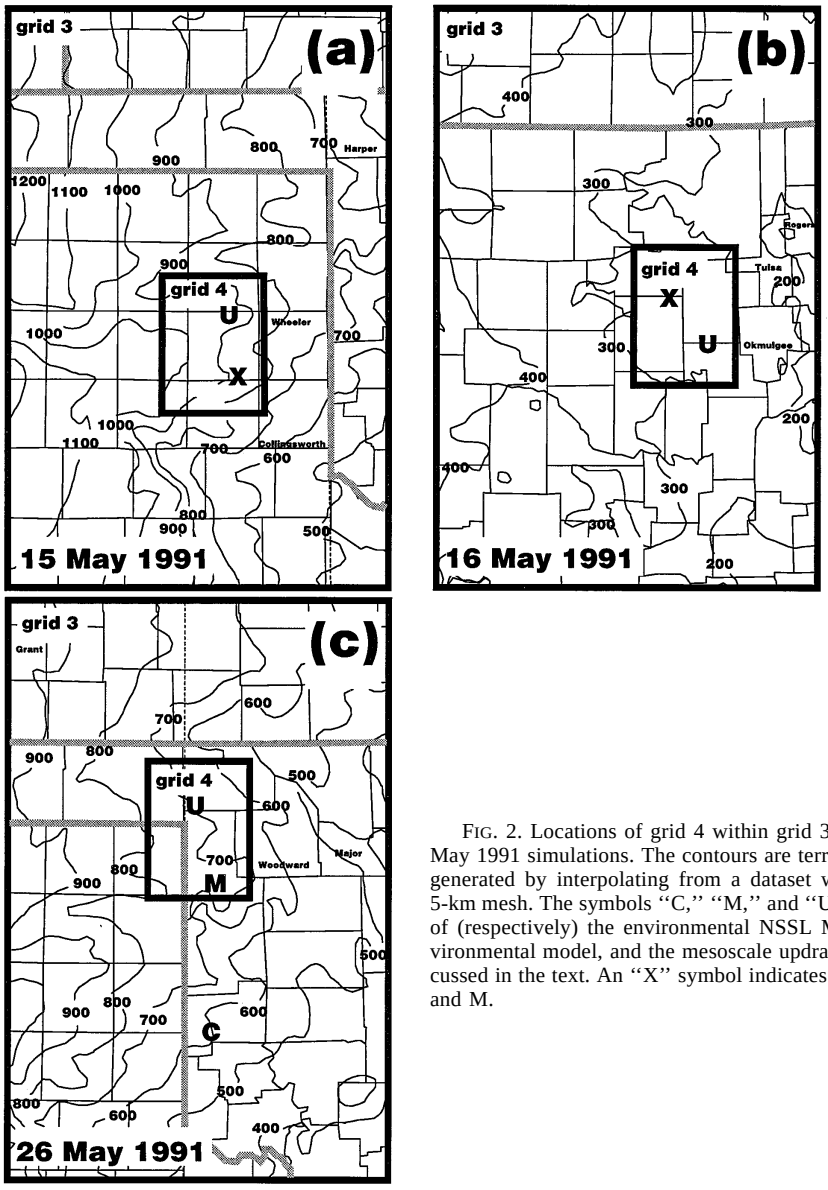

FIG. 2. Locations of grid 4 within grid 3 for the 15, 16, and 26 May 1991 simulations. The contours are terrain on grid 3 (m MSL), generated by interpolating from a dataset with 30″ spacing to the 5-km mesh. The symbols ''C,'' ''M,'' and ''U'' indicate the locations of (respectively) the environmental NSSL Mobile CLASS, the environmental model, and the mesoscale updraft model soundings discussed in the text. An ''X'' symbol indicates collocated soundings C and M.

over northeast Oklahoma for the 16 May case, and over northwest Oklahoma for the 26 May case (Figs. 1 and 2). The gridpoint spacing, indicial and physical dimensions, and time step employed on the various grids have the same values for each case (Table 2). The model terrain is generated by interpolating datasets of either 10′ (e.g., Fig. 1) or 30″ spatial increments (e.g., Fig. 2) to the outer or inner two atmospheric grids, respectively. The soil model is discretized into 11 layers spaced 3 cm apart for a total depth of 0.3 m; there is one soil grid for each atmospheric grid, and the horizontal location of soil and atmospheric grid points are identical.

TABLE 2. Grid parameters for the dryline study.

Grid (number)	Δx (km)	Stretched Δz (km)	Grid dimensions	Δt (s)
Outer (1)	60	• 0.1–1 (0–13 km) • 1 (above 13 km)	45 × 45 × 40 (2640 × 2640 × 20 km)	80
First nest (2)	20	—	53 × 62 × 40 (1040 × 1220 × 20 km)	40
Second nest (3)	5	—	42 × 82 × 40 (205 × 405 × 20 km)	20
Third nest (4)	1	—	72 × 97 × 40 (71 × 96 × 20 km)	5

Although deeper soil layers would probably be necessary for extended integrations on the order of weeks to months, the specified soil layer depth is sufficient for short-period model integrations on the order of one day.

To focus on the initiation and early evolution of the first afternoon dryline convection, we represent convection explicitly on the 1-km grid and do not include subgrid convective parameterizations on the coarser meshes (Table 1). A warm rain cloud microphysical parameterization is chosen for the 1-km grid since it is the simplest optional scheme capable of producing low-level cold pools (which are important for storm propagation). In a future study focusing on the evolution of a mesoscale convective system (MCS), an appropriate set of subgrid convective parameterization schemes could be implemented on the meshes with grid spacings greater than 20 km. In isolated instances our simulations on the 5-km mesh contain rather poorly resolved deep convection, as illustrated later in this paper. Cold outflows from this so-called pseudo-convection could introduce unrepresentative mesoscale forcing of new convection into the calculations on the 1-km grid. To avoid potentially spurious effects, the microphysical processes are deactivated on the coarser meshes with grid spacings of 5 km or greater. (Nonetheless, both condensation at water saturation and radiative effects of clouds are included on all grids.) This treatment of microphysics is justified by the isolated character of the deep convection in the cases studied and, as discussed below, the rather large horizontal extent of the finest grid.

b. Initialization of atmospheric fields

Initial atmospheric fields are generated by blending gridded 2.5° (latitude–longitude) output from the Environmental Modeling Center (EMC) Nested Grid Model (NGM) with upper-air soundings from the synoptic observing network in an isentropic analysis. The isentropic surfaces are spaced at a 1-K interval from ground level through the atmospheric boundary layer, and the spacing between isentropic surfaces increases with elevation above the boundary layer. A two-dimensional objective analysis of surface observations is interpolated to the model grids, while the isentropic analysis is interpolated to the atmospheric grids. To complete the initialization of the atmospheric state, the surface analysis is extrapolated to the gridded atmospheric analysis using a weighting function decreasing from a value of unity at the surface to zero at 500 m above ground level. The Barnes scheme is used to manage the distance-dependent weighting of data in the analyses. The initial vertical motion is set to zero without imposing a balance constraint on the initial mass and horizontal wind field (e.g., Pielke 1984), producing a smooth, noise-free evolution of the model fields after integration begins.

TABLE 3. Values of selected vegetation parameters of the predominant land use types for the dryline study.

BATS land-use category (number)	LAI	Roughness (m)	Albedo (noon)
Crop/mixed farming (1)	6	0.06	0.20
Short grass (2)	2	0.02	0.26
Evergreen needleleaf tree (3)	6	1.00	0.10
Deciduous broadleaf tree (5)	6	0.80	0.20
Tall grass (7)	6	0.10	0.16
Evergreen shrub (16)	6	0.10	0.10
Mixed woodland (18)	6	0.80	0.18

c. Initialization of vegetation and soil fields

The vegetation type in the model is based on the United States Geological Survey (USGS) Earth Resources Observation System (EROS) land use database (e.g., Lee 1992). The USGS dataset contains land use information interpolated to a 1 km × 1 km grid covering the contiguous lower 48 United States. In the first step, each USGS vegetation category is mapped to the appropriate category of the Biosphere–Atmosphere Transfer Scheme or BATS (Dickenson et al. 1986). In the second step, the 1-km land-use data is interpolated to each RAMS grid using a Barnes weighting function, and the predominant BATS category is assigned to each RAMS grid cell. The BATS values of leaf area index (LAI), roughness, and noontime albedo for predominant land use types in our simulations are listed in Table 3. The relative stomatal resistance is modeled as a function of environmental variables as described in Avissar and Mahrer (1988). Crop-mixed farming, short grass, and evergreen shrub categories are predominant over the western portions of the southern Plains (e.g., 15 May case; Fig. 3), yielding to a predominance of crop-mixed farming, with small amounts of short and tall grass, deciduous broadleaf tree, and evergreen shrub, over central and northeastern Oklahoma (not shown). The land use has a patchlike character in all regions.

The soil type is important to the extent that it affects soil moisture and, secondarily, albedo. In particular, the rate at which the soil layer releases moisture to the air is critically dependent on the hydraulic conductivity. Soil type is categorized according to the eleven United States Department of Agriculture (USDA) textural classes including peat (USDA 1951); the physical parameters for the various soil types are discussed by McCumber and Pielke (1981). Aside from either sand or peat, the critical parameters do not exhibit strong dependencies across the range of intermediate soil types. Sandy clay loam, an intermediate USDA soil type, is chosen for the current simulations because it broadly represents soil conditions over the southern Plains. (As the capability to input soil databases into RAMS is under development, variable soil type would be included in follow-on studies.) In any event, we speculate that soil heterogeneity should be a secondary effect compared to

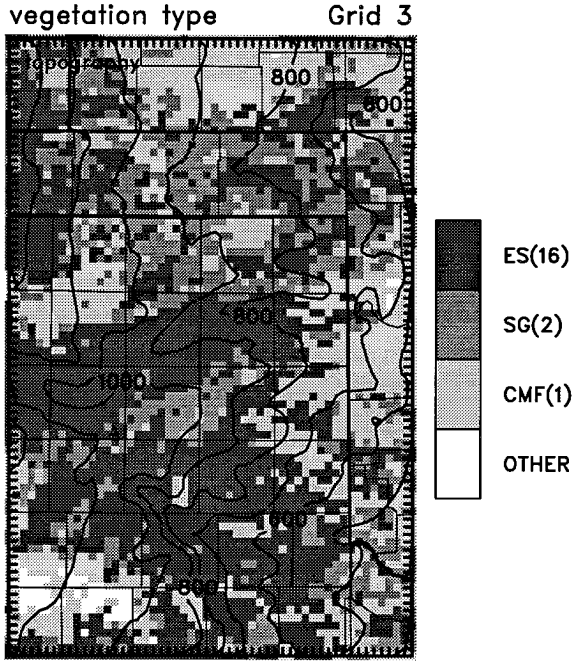

FIG. 3. USGS land cover data on the second nested grid used in the 15 May 1991 dryline simulation. The predominant USGS land cover class is converted to a BATS classification. Each pixel is a 5 km × 5 km grid cell. The gray scales depict the following categories which predominate in the area displayed: crop/mixed farming (CMF); short grass (SG); evergreen shrub (ES); categories other than the first three (OTHER).

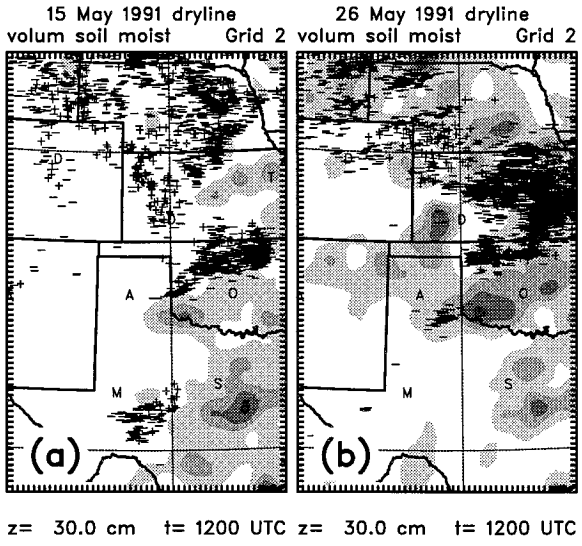

FIG. 4. Soil moisture analyses at lowest model level (soil depth 30 cm); (a) 1200 UTC 15 May 1991; (b) 1200 UTC 26 May 1991. Every fifth lightning ground strike from the National Lightning Detection Network (NLDN) is plotted for the 24-h period beginning at analysis time. Gray scale begins at a volumetric soil moisture of 0.075 m^3 m^{-3} and increments by 0.05 m^3 m^{-3}.

the heterogeneities of soil moisture and vegetation for forcing dryline convection.

The volumetric fraction of soil moisture (i.e., volume of water per volume of water at soil saturation, or simply soil moisture), a dimensionless quantity, is initialized using the antecedent precipitation index (API) technique (Wetzel and Chang 1988). Quoted values of soil moisture are volumetric fractions of field capacity of the assumed sandy clay loam-type soil. In the first step, API values are derived from a three-month-long time series of 24-h total precipitation measurements at each hourly precipitation data (HPD) station. The bulk soil moisture fraction *S*, a percentage of the local field capacity, is then computed from the API value at each rain gauge site and horizontally interpolated to the model grids following the same objective technique as used for the surface data analysis.

Preliminary sensitivity tests in the 15 May case have demonstrated that using 100% of the API soil moisture produces spurious magnitudes of cooling and wind divergence near the surface above moist patches, suggesting that a nonclassical mesoscale circulation (NCMC) is being forced by the reduced sensible heat fluxes there (Segal and Arritt 1992). Specifically, the sensible heat flux becomes small or negative in the core region of the moist patch as warm, relatively dry air advects into the NCMC. It is speculated that the one-level API analysis does not properly account for antecedent drying of upper soil levels that are forcing the NCMC to form. To approximate the effect of antecedent drying of the upper soil layers (e.g., Lee 1992) and to limit the growth of NCMCs to their observed intensities, the actual soil moisture is assigned as a fraction of the API soil moisture, which increases linearly with depth in the soil from 0.2 at the surface to 0.5 at 30 cm. Physical constants of the soil layer on all grids, including such soil-moisture-specific parameters as field capacity and hydraulic conductivity, are based on the assumption of sandy clay loam. The soil temperature profile on all grids is initialized in terms of an offset from the atmospheric surface temperature ranging from 5 K at the surface to 10 K at 30 cm.

The analysis of initial soil moisture at 30-cm depth reveals band- and patchlike features of mesoscale extent and increasing total areal coverage by moist patches from middle to late May (Fig. 4). To assist in interpreting the soil moisture analyses, we employ densely concentrated lightning strike areas as proxies for heavy convective rainfall (Battan 1965; Piepgrass et al. 1982). The soil moisture analysis on 16 May (not shown) is very similar to the analysis on 15 May, except for very modest ''dry-down'' in areas without widespread, persistent deep convection and varying amounts of moistening in regions experiencing storms during the previous 24 h. (Because the HPD stations are not closely spaced enough to adequately sample isolated storms, the API analysis sometimes does not indicate significant moistening from day to day in areas that have just experienced convective rainfall.) The analyses reveal concen-

trated soil moisture patches above which thunderstorms did not subsequently develop, while storms did develop over the dry margins of the moist patches. These relative patterns of soil moisture and storms imply an NCMC-like boundary layer flow regime with divergence above the moist patches on or near the dry margins downstream from the moist patches. From inspection of radar summary charts from mid-April to mid-May 1991, the tracks of MCSs appear to visually correlate with soil moisture bands. The analyzed soil moisture fields on all days are qualitatively consistent with analyses of total precipitation, drought severity, and drought severity index by division (USDOC/USDA 1991a,b).

3. Results

The synoptic environments of the 15–16, 16–17, and 26–27 May drylines were dominated by the confluence of a southerly current carrying moisture from the Gulf of Mexico with dry westerly winds from northern Mexico and the intermountain region of the southwestern United States. As is typical of the southern Plains region around sunrise on days with drylines, the horizontal wind and moisture contrasts were initially rather diffuse. On each day, the confluence zone moved eastward and coincided with a sharpening tendency of the west–east moisture and virtual temperature gradients as the dryline strengthened during the afternoon. From the morning of 15 May to the morning of 16 May, a cold-core 500-mb low pressure center moved from the Utah–Colorado border to southeastern Colorado, while a weak short wave lifted northeastward from Oklahoma into Missouri and Arkansas. From the morning of 26 May to the morning of 27 May, a moderate 500-mb short wave lifted northeastward from Iowa and Illinois and a lesser short wave moved across northwestern Oklahoma from eastern New Mexico, while ridging built slowly northward from Texas. The special mesoscale observations for these cases are described by Hane et al. (1993).

We have made a series of 12-h forecasts for the period 1200–0000 UTC (all times are universal) on 15–16, 16–17, and 26–27 May 1991 using the model configuration and initialization described above. The simulation procedure is nearly identical on all days, the only exception being that the locations of grids 3 and 4 have been subjectively ''optimized'' to place the dryline and subsequent deep convection within their lateral boundaries. We have avoided adding artificial soundings or non–National Weather Service (NWS) data into the initial state or ''tuning'' model parameters to achieve some desired solution in a particular case.

In each case we employ a three-step solution procedure: 1) integrate the model on the outer three grids for 12 h, noting dryline location and the development of regions of convergence, water saturation, and cloud liquid on the 5-km mesh; 2) position the 1-km grid inside the 5-km grid at the time and in the region that either shallow clouds are first noted along the dryline or strong convergence develops on the 5-km mesh, then initialize the fine grid with data interpolated from the 5-km mesh; 3) restart the model from detailed input history files at the time the fourth mesh is spawned and integrate on all four meshes for a period of 3 h (not exceeding the end time of the three-mesh run). The four-mesh, 3-h runs begin at 1900, 2100, and 2000 for the three cases, respectively. Inspection of visible satellite imagery verifies that cumulus convection begins to develop along the dryline at around these times on the respective days. The fourth grid is spawned at the restart time by interpolating variables from the parent 5-km grid, with the exceptions of 1) topography (interpolated from the same 30″ spatially incremented topography as the 5-km grid) and 2) land use (based on the USGS dataset as previously discussed).

An important aspect of the study is the analysis of sounding parameters that indicate the degree of convective instability. Observed soundings are obtained from the National Severe Storm Laboratory Mobile Cross-chain Loran (long range aid to navigation) Atmospheric Sounding System, or M-CLASS (Rust et al. 1990), while model soundings are grid column output. We compute CAPE and CIN following Bluestein and Parker (1993) except that virtual potential temperature is employed in place of potential temperature to compute parcel buoyancy (Doswell and Rasmussen 1994) and the lower limit of integration for the CIN computation is the level of parcel origin instead of ground level. We assume two alternative approaches to define source air parcels for initial cumulus convection: 1) a lifted parcel has the average properties of the lowest 75 mb of the sounding and begins ascending at the layer averaged pressure and 2) the lifted parcel originates from and has thermal properties of the level of the virtual potential temperature θ_v minimum at the top of the superadiabatic layer (i.e., removes effects of the superadiabatic layer near the ground). The lifting of the minimum virtual potential temperature parcel, predicated on the notion that thermals originating in the surface layer do not initiate deep convection in the absence of significant mesoscale lifting, approximates the maximum CIN possible.

a. 15 May 1991 dryline

A sharply defined dryline developed on the afternoon of 15 May 1991 in the eastern Texas panhandle (Fig. 5a) and has been simulated by the model (Fig. 6a). This classic dryline is marked by large dewpoint temperature gradients and strong low-level airflow convergence, as was verified by National Oceanic and Atmospheric Administration (NOAA) P-3 aircraft stepped traverses, serial M-CLASS soundings released on both sides of the dryline, and National Center For Atmospheric Research (NCAR) Portable Automated Mesonetwork (PAM) surface measurements (Hane et al. 1993). The advance of the dryline is slowed in the eastern Texas Panhandle as

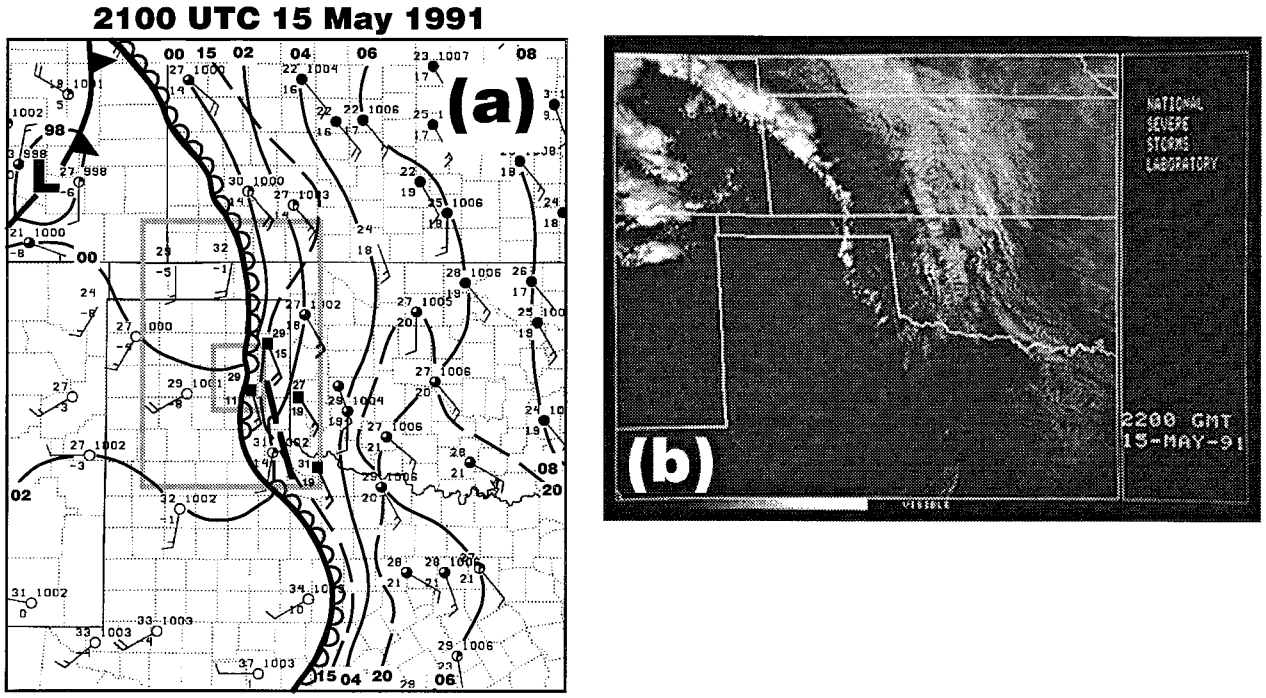

FIG. 5. Observed weather conditions on the afternoon of 15 May 1991. (a) Surface analysis at 2100 UTC; (b) visible satellite imagery at 2200 UTC. The station model in panel (a) includes (counterclockwise from upper left) temperature (°C), dewpoint temperature (°C), and MSL pressure (mb), as well as winds and cloud cover. An NWS site is denoted by a circle, while a square denotes an NCAR PAM site. Boundaries include dryline (scalloped curve), cold front (filled-barbed curve), and trough (dashed curve).

a developing low pressure center over the Colorado Rocky Mountains backs and strengthens the low-level winds over the southern Plains. Additional sensitivity tests, which have assumed soil moisture ranging from 100% of the API-based values to a homogeneously dry state, suggest that the action of the aforementioned NCMC mechanism is to reduce the eastward movement of the dryline by increasing low-level convergence on the west flank of the moist patch in southwest Oklahoma (Shaw 1995). Another study of the 15 May case by Grasso (1996) has explored the development of strong vertical rotation in simulated dryline convection.

A band of cumulus convection began to develop along the dryline during the early afternoon, producing small storms by late afternoon (Fig. 5b), which spawned several funnel clouds (Bluestein 1994). The locations of lightning activity from the observed dryline storms are within a few tens of kilometers east of the simulated dryline position during their early development (Fig. 6a). In the model output on the 5-km mesh, ''pseudo-convection'' develops along the dryline at locations of moisture convergence maxima (Fig. 6b). These dryline storms subsequently propagated eastward away from the dryline and into deeper moisture, producing severe weather (USDOC 1991) including F-3 tornadoes in northwestern Oklahoma (0135–0211) and in the eastern Texas panhandle (0217–0310). The tornado locations are outside grid 4 but within the boundary of grid 3 (Fig. 2a). Other storms were observed along the dryline in western Kansas.

On the 1-km mesh, simulated cumulus convection is initiated along the dryline in bands characterized by convergence, high precipitable water content, low CIN, and updrafts to 5 m s^{-1} (Figs. 7a,b). The convergence bands correspond to features developing on the 5-km grid (e.g., Fig. 6a), although their intensity is greatest on the fine mesh due to improved spatial resolution there. Using CIN computed from the level of minimum θ_v, it is apparent that cloudy areas possess low CIN values while cloud-free areas have high CIN values (Fig. 7b). (The field of CIN computed more conventionally from a parcel averaged over the lowest 75 mb reveals similar trends but smaller absolute differences between cloud bands and cloud-free areas, owing to the influence of the superadiabatic layer.) The CBL reveals bulges or hummocks of moisture and θ_v collocated with deep, concentrated convergence and updrafts (Figs. 7c,d). The locations of the thermal plumes coincide with the bands of low CIN. Cumulus convection is in early stages of formation near the tops of the mesoscale updrafts and moisture bulges.

A comparison of M-CLASS and grid 4 model output soundings, located as in Fig. 2a, reveals a rather well-mixed CBL that possesses a superadiabatic layer above the surface and a large negative lapse rate of vapor mixing ratio (Fig. 8). The soundings are located east of

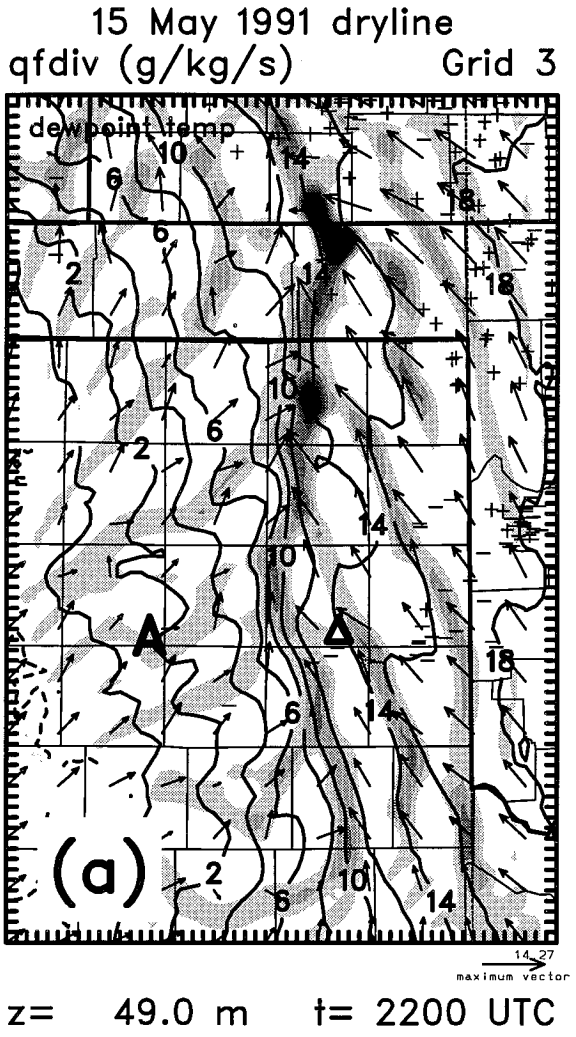

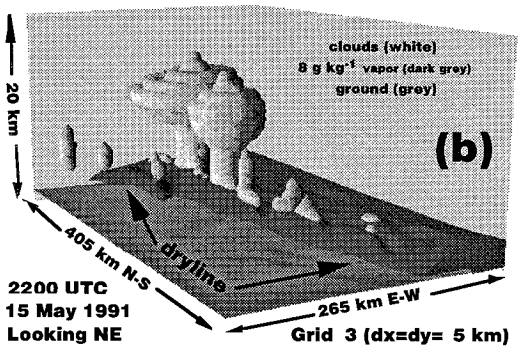

FIG. 6. Model output on grid 3 at 2200 UTC for the 15 May 1991 simulation. (a) Vapor mixing ratio flux convergence (gray scale starting at 1×10^{-3} g kg^{-1} s^{-1} and increasing convergence at an increment of 3×10^{-3} g kg^{-1} s^{-1}) and airflow vectors; (b) surfaces of cloud and 8 g kg^{-1} vapor mixing ratios in perspective view of entire grid 3 domain. Every lightning ground strike from the NLDN is plotted for the 9-h period beginning at 1800 UTC. In panel (a), the symbol "A" locates the Amarillo NWS office while the triangular symbol collocates M-CLASS and modeled dryline environmental soundings discussed in the text.

the dryline in a region with weak horizontal moisture gradients and airflow convergence and high CIN values.

b. 16 May 1991 dryline

A dryline extended into northeastern Oklahoma and south-central Kansas on the afternoon of 16 May 1991 (Fig. 9a), and has been simulated by the model (Fig. 10). The eastward bulge of the dryline is assisted by southwesterly geostrophic winds, which strengthen during the day as a synoptic-scale upper low pressure center moves from Colorado into southwest Kansas. The advance of the dryline is also assisted by downward momentum mixing from midtroposphere (Koch and McCarthy 1982). The northeastward advance of the dry air forms a dry slot southeast of the upper low that increases dewpoint contrasts across the dryline during late afternoon (Fig. 10).

Isolated areas of cumulus convection were observed to form along the dryline in southern Kansas and northeastern Oklahoma during midafternoon, eventually developing into supercell storms over southern Kansas and near Tulsa, Oklahoma (Fig. 9b). The locations of lightning activity from the two observed dryline storms are within a few tens of kilometers east of the simulated dryline position during their mature stages (Figs. 9b, 10). The Oklahoma storm produced severe weather in northeastern Oklahoma (USDOC 1991), including two F-1 tornadoes (2309–2325 and 2320, respectively), an F-0 tornado (2308), and an F-2 tornado (0136–0140). The tornado locations are just outside grid 4 but within the boundary of grid 3 (Fig. 2b). Other storms developed at the intersection of the dryline with the thunderstorm outflow boundary in southwest Kansas.

Special sounding and mobile mesonet observations from the M-CLASS vehicle reveal conditions at the dryline just west of the severe Oklahoma convection and illustrate the rather good accuracy of the 12-h forecasted dryline position. By late afternoon, the M-CLASS vehicle had penetrated the dryline between Norman and Tulsa and set up a sounding site at the location shown in Fig. 2b. The location of the evening M-CLASS

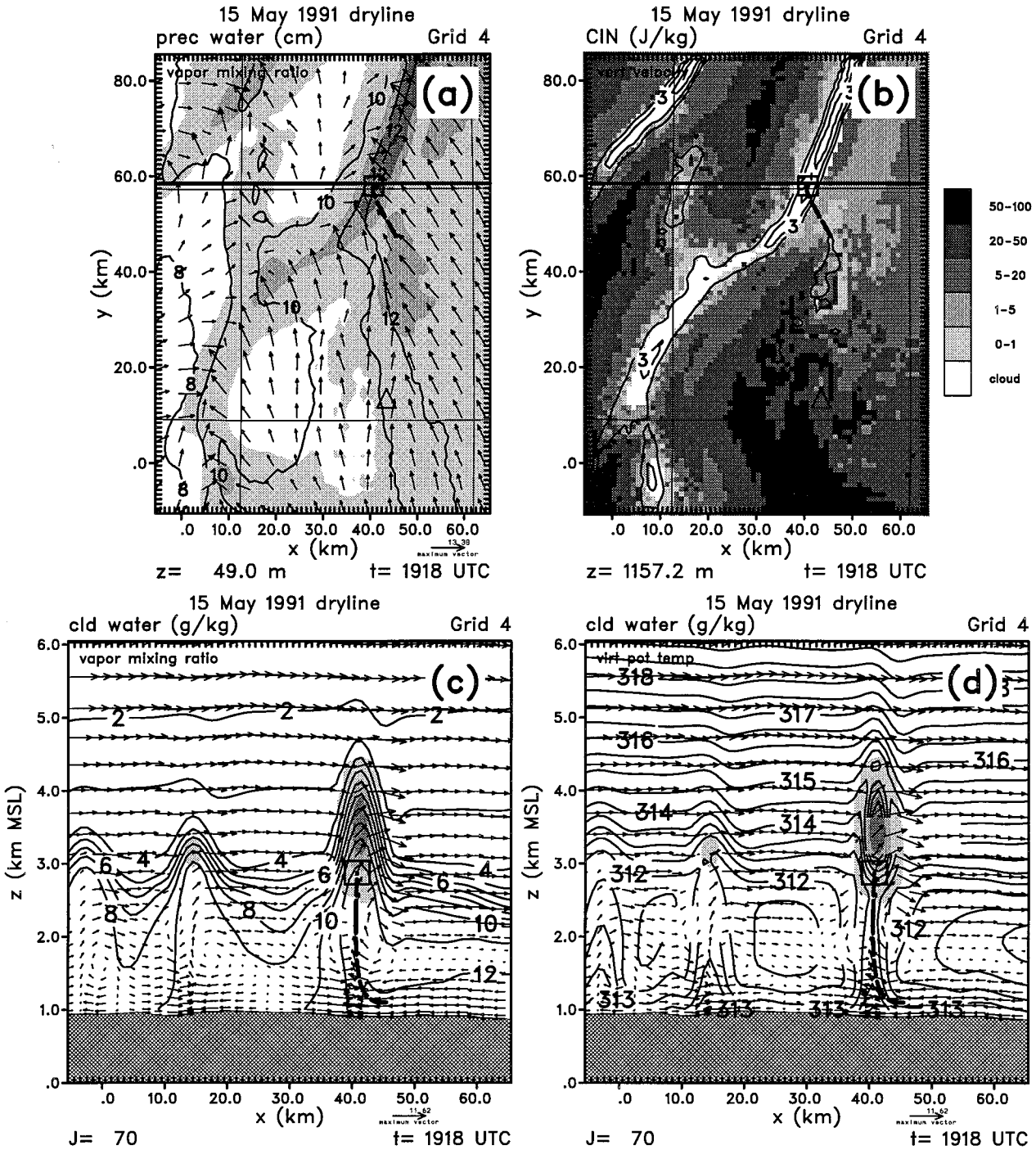

FIG. 7. Model output on grid 4 at 1918 UTC for the 15 May 1991 simulation. Panels (a) and (b) are horizontal sections, while panels (c) and (d) are vertical west–east cross sections located by the bold lines in (a) and (b). (a) Precipitable water (gray scale starting at 2.5 cm and increasing at an increment of 0.5 cm), contoured vapor mixing ratio (g kg^{-1}), and vectors at 49 m AGL; (b) CIN in J kg^{-1} (each grid square filled according to the gray scale at right) and contoured positive vertical velocity at 1157 m AGL (beginning at 1 m s^{-1}, increasing at 2 m s^{-1} interval); (c) cloud water mixing ratio in g kg^{-1} (gray scale starting from zero and increasing at an increment of 0.5 g kg^{-1}), contoured vapor mixing ratio (g kg^{-1}), and airflow vectors; (d) cloud water mixing ratio (g kg^{-1}), contoured virtual potential temperature (K), and airflow vectors. White areas in panel (b) indicate presence of clouds in the column. Every fifth gridpoint vector is plotted in (a), while every vector vertically and every other vector horizontally is plotted in (c) and (d). The heavy dashed curve locates an air trajectory computed using the spatial interpolation scheme of Ziegler et al. (1983) at a 1-min time step from 6-min-interval model output from 1900 to 1924 UTC. The box symbol locates the endpoint of the trajectory.

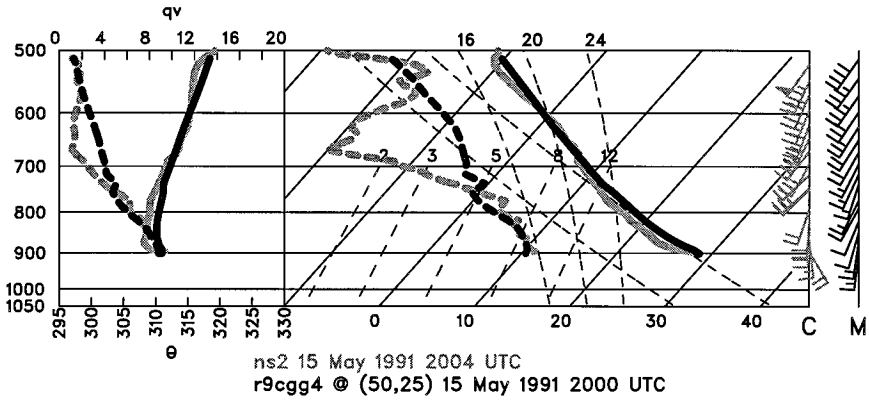

FIG. 8. Skew *T*–log*p* diagram of observed and model soundings on the afternoon of 15 May 1991. The first listed sounding (gray) is an NSSL Mobile-CLASS sounding (C), the second (black) is a model sounding (M), and C and M are collocated east of the dryline. Sounding locations are plotted in Fig. 2. Solid curves denote temperature, while dashed curves denote dewpoint temperature.

sounding site (triangular symbol in Fig. 10) is within the simulated dryline zone, which is consistent with the dryline having been traversed earlier to the west and observed deep convection feeding on deeper moisture to the east of the sounding site. The deep convection near Tulsa developed just east of the dryline, and both the deep convection and a shallow cumulus cloud band were visually observed to the east of the sounding site around 0000 in accord with satellite imagery (Fig. 9b).

Shallow modeled cumulus convection is first initiated along the dryline around 2130 in bands with low CIN, high values of θ_v and precipitable water content, and boundary layer updrafts of over 3 m s^{-1} (Fig. 11). The timing of simulated convective initiation is in good agreement with the observed onset of convection around 2100.

The collocated soundings from the M-CLASS and grid 4 model output at around 0000 reveal a rather well-mixed boundary layer with vapor mixing ratios in the 8–10 g kg^{-1} range (Fig. 12). The simulated low-level

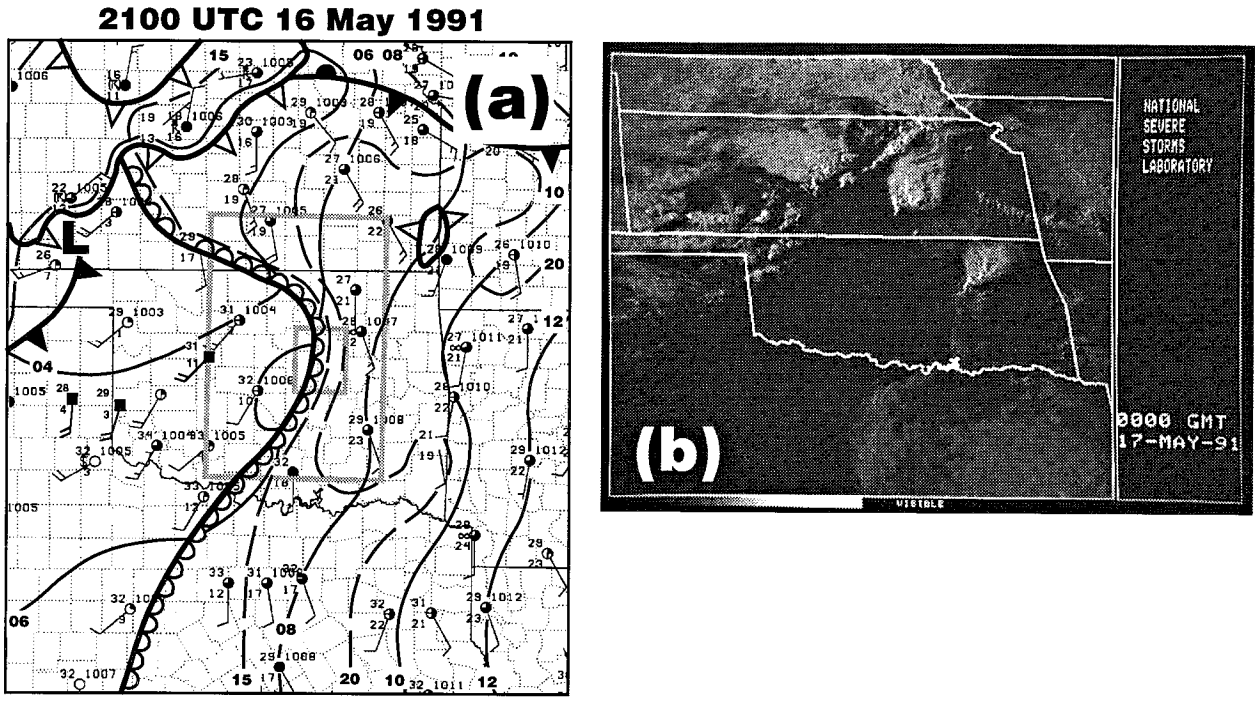

FIG. 9. Same as in Fig. 5 but for 16 May 1991 case and satellite imagery at 0000 UTC 17 May. Warm front (filled-scalloped curve); outflow (open-triangled curve).

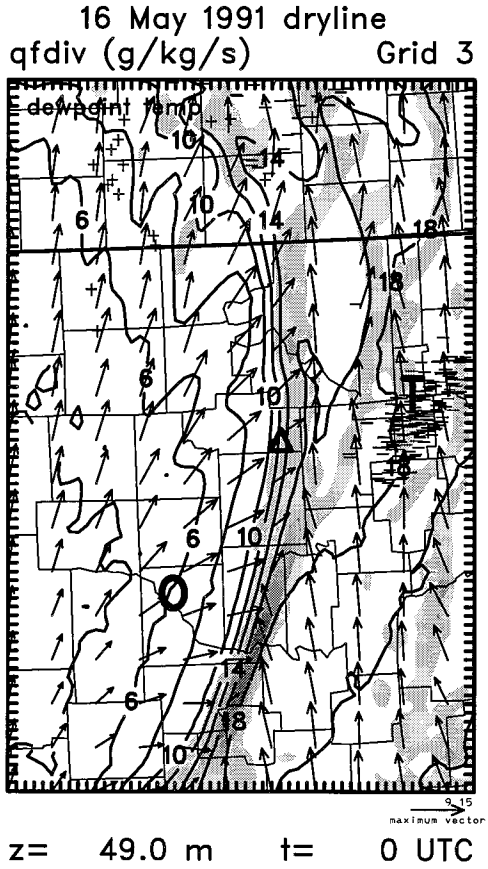

FIG. 10. Same as in Fig. 6a but for 16 May 1991 simulation and output at 0000 UTC 17 May. The symbols ''O'' and ''T'' locate the Norman and Tulsa NWS offices, while the triangular symbol collocates M-CLASS and modeled dryline environmental soundings discussed in the text.

winds are more westerly and vapor mixing ratios are somewhat lower in comparison to M-CLASS measurements, probably because the western edge of the simulated dryline zone is just east of the sounding site. The simulated wind and moisture profiles in the lowest 300 mb are indicative of the entrainment of dry air below and detrainment of moist air aloft that are characteristic of the secondary circulation at the dryline location. This relationship between the wind shear and moisture profile at the dryline is also evident in Fig. 11c in the lowest 1500 m of the easternmost moisture bulge.

c. 26 May 1991 dryline

A dryline developed in the eastern Texas panhandle and northwestern Oklahoma on the afternoon of 26 May 1991 (Fig. 13a), and has been simulated by the model (Fig. 14). This dryline is characterized by narrow zones of moderate dewpoint temperature gradients and strong low-level airflow convergence within a broader gradient zone, as also indicated by M-CLASS soundings, PAM mesonetwork measurements, and horizontal sawtooth and stepped traverses by the NOAA P-3 (Hane et al. 1993).

Cumulus convection began to form along the dryline during the early afternoon, leading to the development of a tornadic supercell storm in northwestern Oklahoma and several nonsevere thunderstorms in the southeastern Texas panhandle and southcentral Kansas (Fig. 13b). A second tornadic supercell in southwestern Kansas had originated near high topography in southeastern Colorado and subsequently moved eastward into southwestern Kansas, paralleling but north of the midafternoon dryline, which recurved sharply westward along the Kansas border. The locations of lightning activity from the dryline storms are within a few tens of kilometers of the simulated dryline position during their early development (Fig. 14). These storms eventually produced severe weather (USDOC 1991), including an F-1 tornado in southwestern Kansas (2255) as well as an F-3 and two F-1 tornadoes (2335–0018) and an F-0 tornado (0201) in northwestern Oklahoma. The tornado locations are within the boundary of grid 3 but outside of grid 4 (Fig. 2c), although the early stage of the storm producing the F-3 tornado occurred within the eastern portion of the fine mesh.

Cumulus convection begins to develop along the dryline in the northeastern Texas panhandle and northwestern Oklahoma around 2000 in both the simulation and the observations. A shallow cumulus band has just been initiated along the dryline in an area with low CIN, high values of θ_v and precipitable water content, and boundary layer updrafts of over 3 m s^{-1} (Fig. 15).

Midafternoon soundings from both M-CLASS and grid 4 model output, located as in Fig. 2c, reveal a rather well-mixed CBL with vapor mixing ratios in the 8–12 g kg^{-1} range and a pronounced humidity lapse rate. An elevated moist layer develops above the 800-mb level, and a superadiabatic layer is noted near the surface (Fig. 16). Both soundings are located east of the dryline, the environment of the model sounding being characterized by weak horizontal moisture gradients and airflow convergence and high CIN values.

4. Discussion

a. Development of boundary layer convergence

Long, narrow bands of moisture convergence, apparently of critical importance for convective initiation at the dryline, are prominent simulated boundary layer features (Figs. 6a, 10, and 14). Here, we distinguish between the dryline, the curvilinear boundary possessing absolute maxima of moisture convergence and humidity gradients (centrally located in Figs. 6a, 10, and 14), and the relatively weak quasi-linear convergence bands that occasionally intersect and develop on either side of the dryline. [In some cases there may be multiple convergence bands, suggesting the notion of ''multiple drylines,'' embedded in a rather diffuse zone of west-

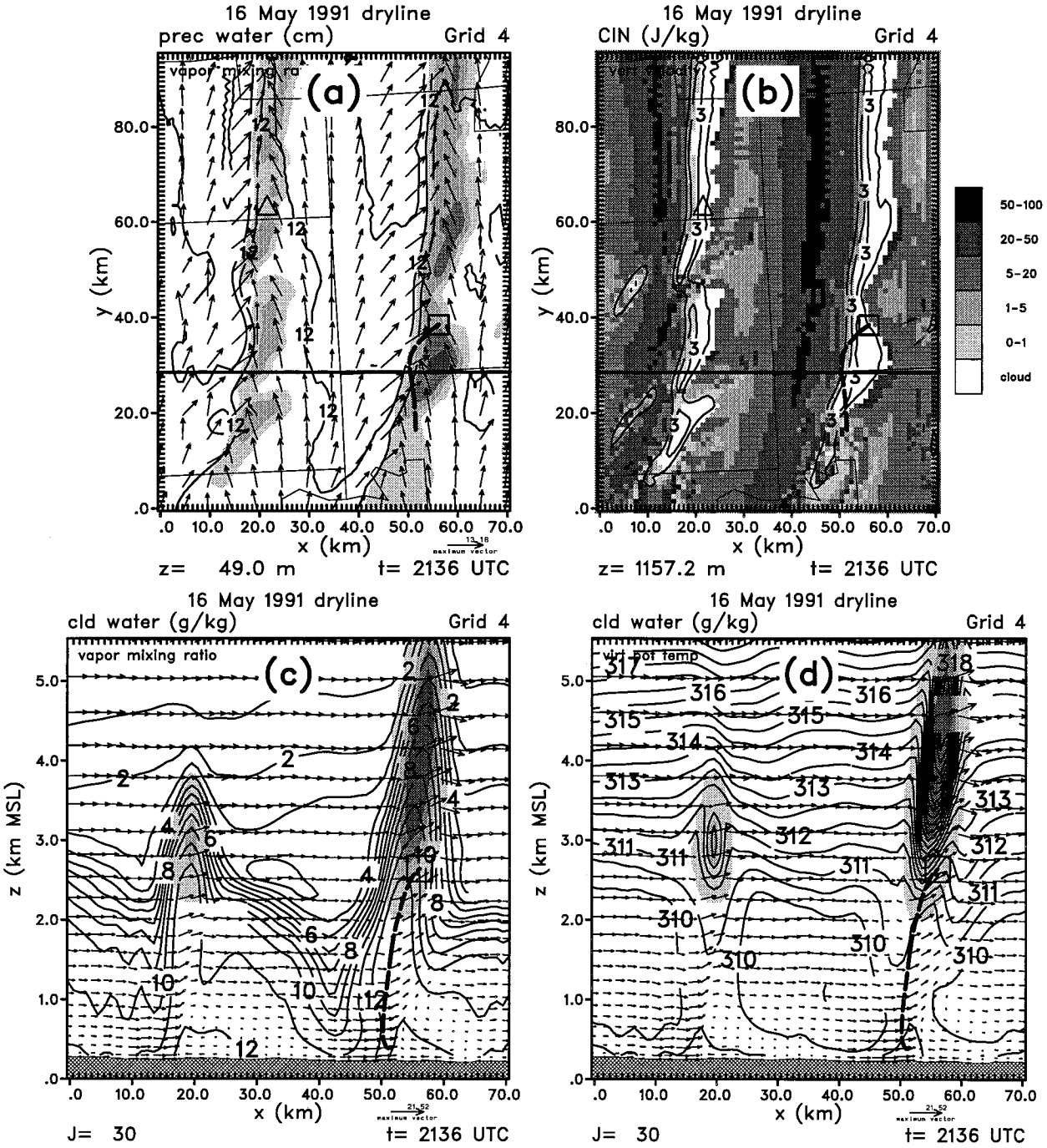

FIG. 11. Same as in Fig. 7 but for 16 May 1991 simulation and output at 2136 UTC 16 May. Precipitable water gray scale starts at 3.5 cm, while air trajectory is from 2100 to 2142 UTC.

to-east moisture increase; see related discussion in Hane et al. (1993).] Strong convergence collocates with maximum thermal gradients at the dryline, while a virtual temperature gradient and cooler air exist to the east of the dryline (Figs. 7d, 11d, and 15d). Inspection of additional model output shows that this arrangement of mass and momentum fields persists in the vicinity of the dryline throughout its development. In accord with the findings of Ziegler et al. (1995), which included explicit calculation of frontogenetic and vorticity dynamical forcing, these fields of airflow and virtual temperature indicate that the drylines in the present study are also thermally direct, solenoidally forced, frontogenetic secondary circulations.

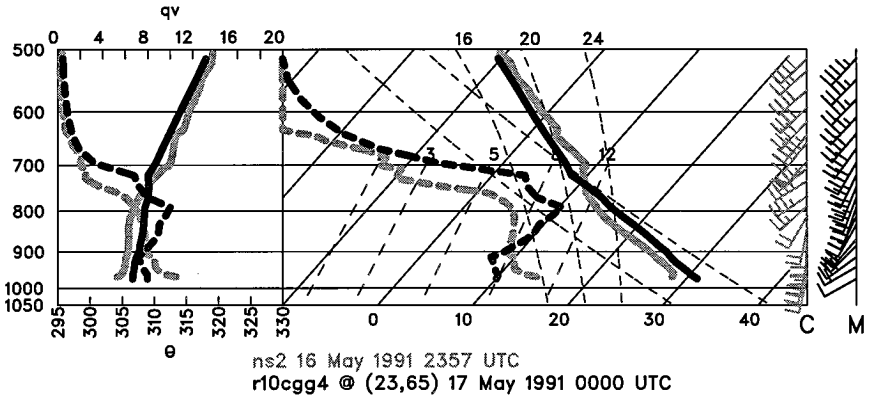

FIG. 12. Same as in Fig. 8 but for 16 May 1991 case. Soundings C and M are collocated and in the immediate vicinity of the dryline.

Maximum simulated updraft speeds along the dryline on the finest grid are in the 2–5 m s^{-1} range (Figs. 7b,c; 11b,c; 15b,c), in good agreement with observations in these and other dryline cases (Hane et al. 1993; Parsons et al. 1991; Ziegler and Hane 1993). On the 5-km grid in the present study, as in Ziegler et al. (1995), the maximum updrafts are around 1 m s^{-1} due to the rather coarse resolution of convergence and frontogenesis. The simulated updrafts are in the range of 3–9 km in width and are up to 100 km or more in length. Our results contain many small amplitude undulations along the simulated drylines (Figs. 6a, 10, and 14), with shapes that are broadly comparable to ''mesoscale dryline waves'' (MDLWs) deduced by McCarthy and Koch (1982) and Koch and McCarthy (1982).

Several other studies have concluded that focused boundary layer convergence and vertical motion may develop via solenoidally forced, convergent, frontogenetic circulations along fronts, sea breezes, or drylines (Ogura and Chen 1977; Koch and McCarthy 1982; Koch 1984; Carbone et al. 1990; Nicholls et al. 1991; Pielke et al. 1991a; Parsons et al. 1991; Ziegler and Hane 1993). Alternatively, localized convergence and vertical motion may arise from isallobaric flow toward locally falling pressure (McCarthy and Koch 1982), gravity waves (Koch and McCarthy 1982) and interaction of

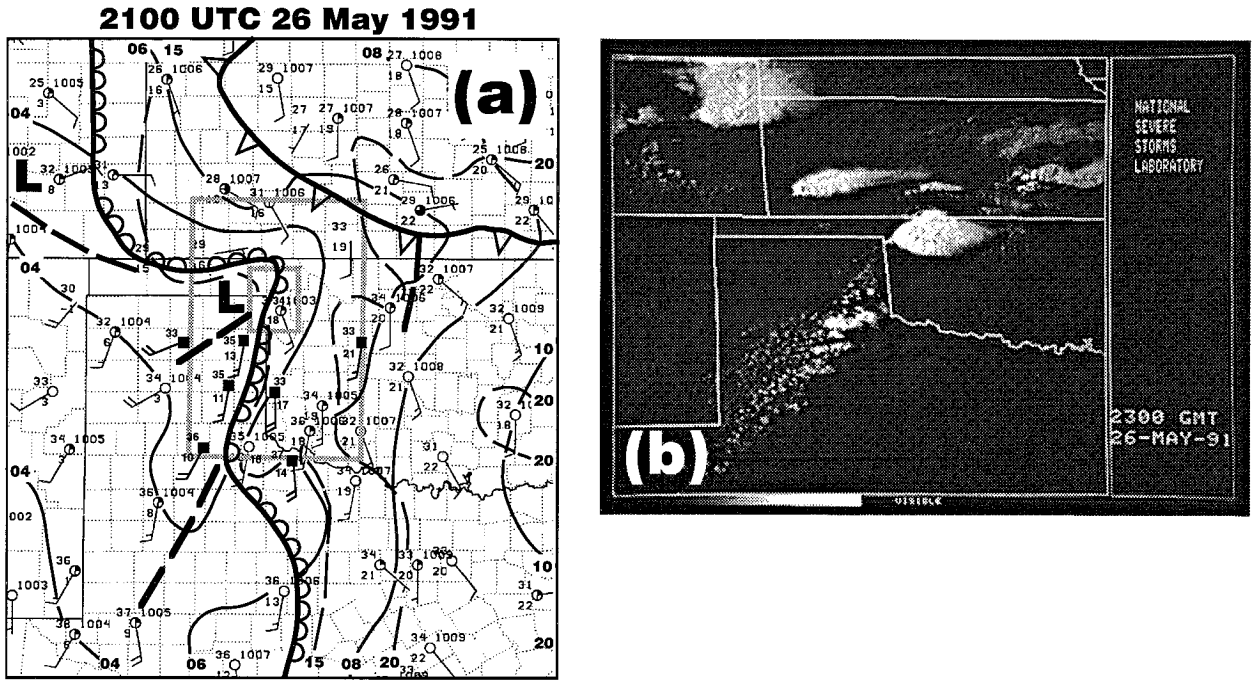

FIG. 13. Same as in Fig. 5 but for 26 May 1991 case and satellite imagery at 2300 UTC 26 May. Outflow denoted by open-triangled curve.

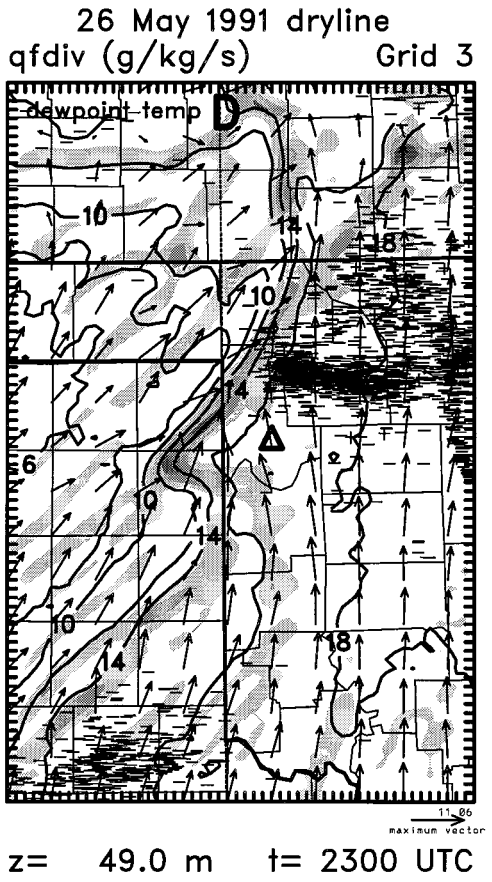

FIG. 14. Same as in Fig. 6a but for 26 May 1991 simulation and output at 2300 UTC 26 May. The symbol ''D'' locates the Dodge City NWS office, while the triangular symbol locates the modeled dryline environmental sounding discussed in the text.

undular bores with the dryline (Karyampudi et al. 1995), differential downward momentum mixing (Ogura and Chen 1977; McCarthy and Koch 1982), symmetric instability (Ogura et al. 1982), or differential surface frictional stress (Weston 1972). A combination of cloud forcing from thermally direct boundary layer circulations and gravity waves has also been proposed (Balaji and Clark 1988).

Other simulated convergence bands develop on either side of the dryline in convectively unstable boundary layers characterized by moderate speed and directional wind shear. These convergence bands are, as the simulated drylines, manifestations of horizontal boundary layer roll vortices. In such environments linear theory of inflection-point or convective instability predicts development of roll circulations with spacings between 2 and 4 times the boundary layer depth, or equivalently ''aspect ratios'' of 2–4, that are aligned with the mean wind (e.g., Brown 1980). These classic HCRs are frequently observed, and their dynamics have been extensively explored.

It is of considerable interest that the simulated convergence bands on either side of the drylines in Figs. 6a, 10, and 14 at least superficially resemble classical HCRs, since they appear only in the CBL, appear roughly parallel to the mean wind, and have fairly regular spacings. The simulated roll circulations are spaced from 15 to 45 km apart in CBLs ranging up to roughly 2 km in depth (i.e., aspect ratios of 7–23). Since the simulated roll aspect ratios lie well outside the predicted range, the simulated convergence bands cannot be explained by classic linear theory. The 5-km grid in the present study is of insufficient spatial resolution (and the 1-km grid has marginal spatial resolution) to simulate classical HCRs.

A recent review paper by Etling and Brown (1993) interprets observations of roll vorticies whose aspect ratios of 4–15 significantly exceed the theoretical limit of 2. Citing recent studies, Etling and Brown propose several possible causes of these ''large-aspect ratio'' roll vortices, including vortex pairing or merger and interactions with gravity waves in the free troposphere. They speculate that ''observed cloud streets are just flow visualizations of a multi-scale boundary-layer process containing dynamic and thermal instabilities as well as nonlinear interactions between various scales of motion.'' Etling and Brown conclude that ''a single instability mode cannot explain the observed structure of large roll-like eddies in the real PBL.''

The convergence bands on either side of the drylines in the present study should be difficult to infer in satellite observations, if in fact present, due to the higher observed frequencies of cloud formation along than away from the dryline. In the 16 May dryline case, the Twin Lakes (OKC) WSR-88D radar indicates a persistent double fine-line echo between Oklahoma City and Tulsa during late afternoon (Fig. 17). The double fine line echo is near the positions of the dryline simulated on the 5-km mesh (Fig. 17) and the quasi-stationary dryline as determined from a stepped traverse of the NOAA P-3 (Hane et al. 1993). Three other fine line radar echoes are observed in central Oklahoma to the west of the dryline (Fig. 17), in the region where weak moisture convergence bands are simulated (as manifested by dewpoint temperature oscillations normal to the flow at lower left of Fig. 10). If the radar-indicated fine lines are caused by the upwelling of insects in the mesoscale updrafts (Wilson et al. 1994), then their detection suggests that the simulated boundary layer convergence bands may have a natural analog.

All simulated convergence bands (including drylines) are characterized by a narrow plume of rising warm air. These warm plumes separate broad regions of sinking air that are relatively cool from the surface through the middle levels of the boundary layer (Figs. 7d, 11d, and 15d). The horizontally convergent inflow toward the local thermal maximum at the convergence line implies that a horizontal heat flux due to resolvable, meso-γ and meso-β scales of motion (i.e., horizontal ''mesoscale fluxes;'' see Pielke et al. 1991b) opposes the vertical mesoscale and subgrid-scale heat fluxes by transporting

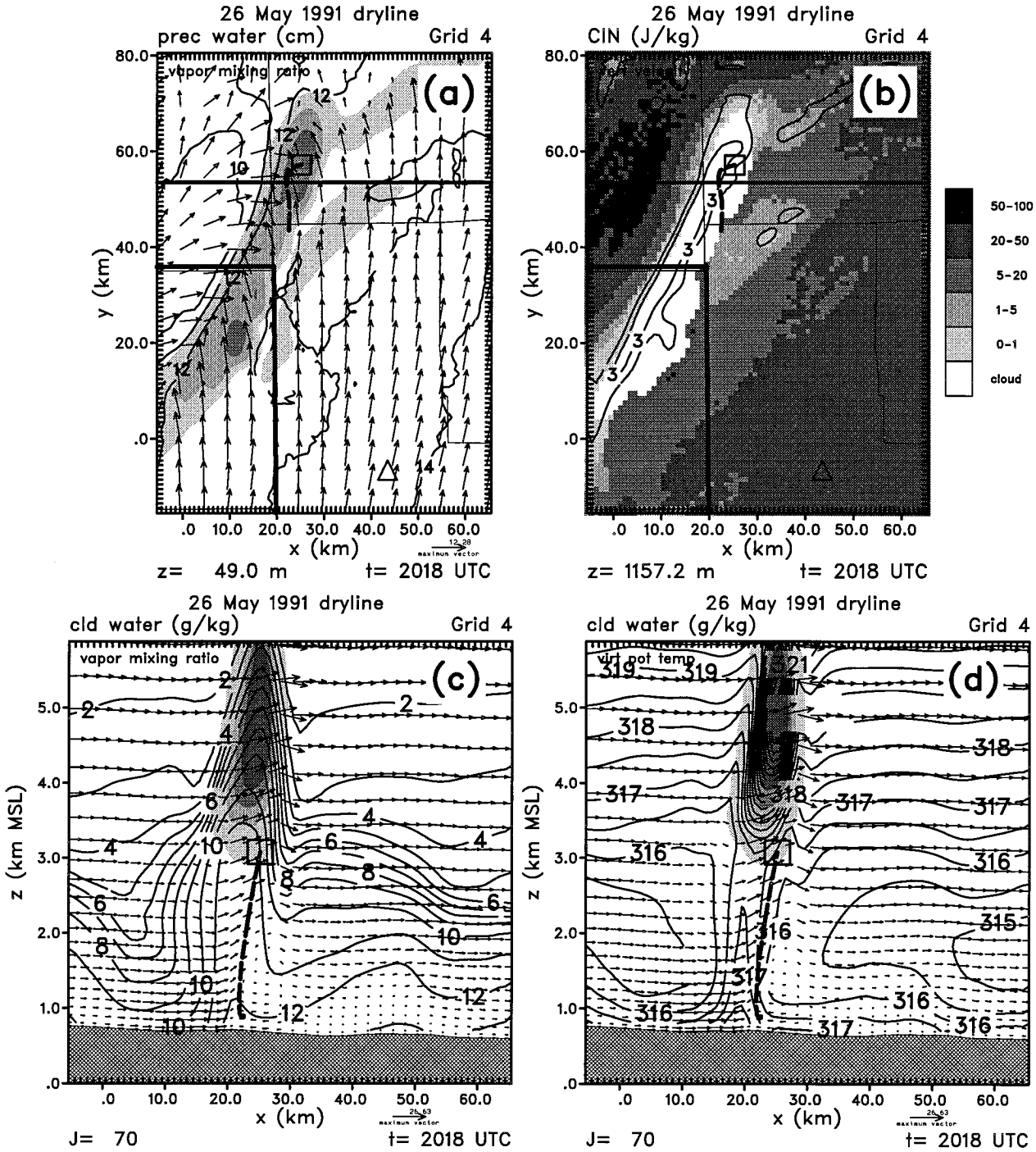

FIG. 15. Same as in Fig. 7 but for 26 May 1991 simulation and output at 2018 UTC 26 May. Precipitable water gray scale starts at 3.5 cm, while air trajectory is from 2000 to 2030 UTC.

relatively cool air toward the convergence axis. The effect of this mesoscale flux is to "flush" the lower boundary layer and maintain a horizontal θ_v gradient. As a result, the highest θ_v values in the simulations tend to be located along the dryline in accord with the observational findings and theoretical considerations advanced by Koch and McCarthy (1982).

b. Role of the mesoscale updraft in the initiation of dryline convection

Cumulus convection develops from the top of the CBL along narrow mesoscale updraft bands coinciding with the dryline location. The CBL reveals bulges or hummocks of moisture and θ_v collocated with deep, con-

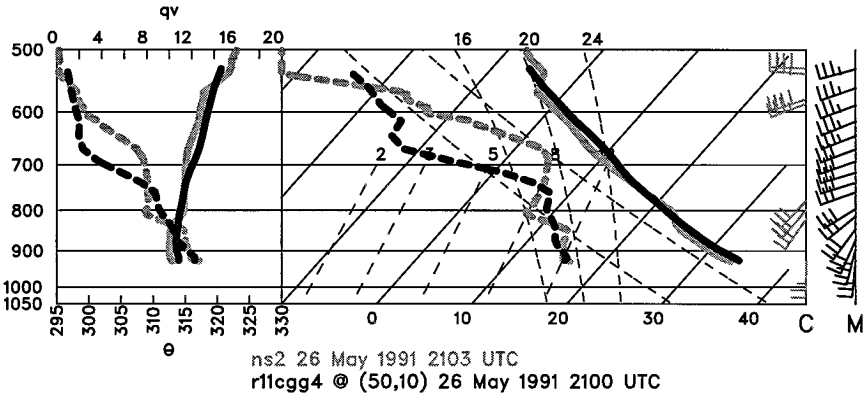

FIG. 16. Same as in Fig. 8 but for 26 May 1991 case. Sounding M is near the southern boundary of grid 4 while sounding C is in the southern portion of grid 3 (see Fig. 2).

centrated convergence (Figs. 7c,d; 11c,d; 15c,d). In all cases, the cumulus convection forms near the top of the mesoscale updrafts and moisture bulges, while thermal plumes coincide with the bands of low CIN marking the dryline. Since a mesoscale updraft band is oriented with a component along the boundary layer wind shear, moist air parcels are gradually lifted over along-band horizontal distances greater than the width of the band itself. A more detailed analysis of air trajectories, which are displayed in Figs. 7, 11, and 15, shows that the mesoscale updraft band feeds air from low levels southeast of the band into the moisture bulge owing to band-normal low-level convergence. To an observer at the convergence band looking in the downwind direction, moist air passes from right to left at low levels beneath the right flank (roll) vortex before rising from left to right under the influence of the cross-band wind shear component. Inspection of Figs. 7, 11, and 15 suggests that other air trajectories that originate at low levels on the western edge of a moisture convergence band would slope rather steeply to the east as the air rises from left to right across a band (see also Ziegler et al. 1995; Fig. 9).

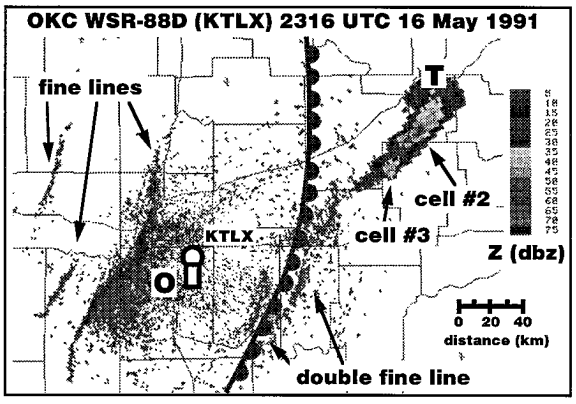

FIG. 17. Base scan reflectivity (dBZ) in storm mode of the WSR-88D radar KTLX northeast of Norman, Oklahoma (''O''), at 2316 UTC 16 May 1991. The heavy scalloped curve denotes the location of the simulated dryline on grid 3 at 2300 UTC 16 May. Radar reflectivities in storms southwest of Tulsa, Oklahoma (''T''), exceed 55 dBZ, while boundary layer echoes away from storms locally maximize in the 5–15-dBZ range.

Since the condensation pressure p^* (Betts and Ball 1995) lowers from right to left toward the warm, dry side of the band, an air parcel originating on the dry side has a higher LCL than a moist air parcel. As latent heating augments the virtual buoyancy in rising cloudy air, the cloud enters it's active stage as the LFC is quickly achieved. Over the relatively large areas between significant updrafts, downward motion, and entrainment of warm dry air into the upper boundary layer prevents the development of cumulus convection by decreasing the boundary layer relative humidity, increasing p^*, and elevating the LCL through the boundary layer top.

The lifting of moist air through the LCL and LFC in the simulations depends on the initial value of p^* and its tendency following the motion of an air parcel rising through the mesoscale updraft. Outside the simulated mesoscale updraft bands and in areas where horizontal fluxes are relatively small, p^* experiences a large diurnal decrease and the total lift needed to saturate surface air parcels experiences a large diurnal increase due to boundary layer mixing and top-down entrainment of dry air. Large diurnal changes of p^* and lift needed to achieve saturation have been reported for observed CBLs by Betts and Ball (1995). Within the mesoscale updraft bands, strong horizontal moisture convergence suppresses the diurnal increase of p^* and increases the probability of initiating cumulus convection. If p^* remains lower than the pressure at all points along a rising trajectory, as may occur either if p^* is initially too small or mixing with potentially warm, dry air lowers p^* following the motion, cumulus convection cannot form.

In comparison to the soundings east of the dryline, model soundings through the mesoscale updraft band reveal much higher moisture values and nearly homogeneous moisture profiles in the boundary layer (Fig. 18). That the lapse rates of potential temperature and

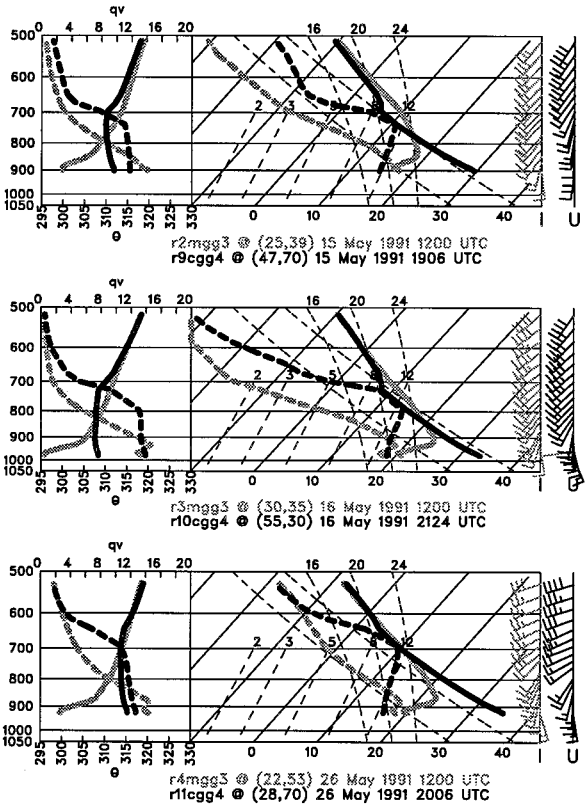

FIG. 18. Skew *T*–log*p* diagrams of model soundings at the mesoscale updraft location (U) indicated in Fig. 2 at initialization (gray) and during the afternoon (black). Top panel: 1200 and 1906 UTC 15 May 1991; middle panel: 1200 and 2124 UTC 16 May 1991; bottom panel: 1200 and 2006 UTC 26 May 1991. Solid curves denote temperature, while dashed curves denote dewpoint temperature.

humidity for air parcels in the mesoscale updraft are small implies that the mixing process does not appreciably warm and dry an air parcel following the motion to cause $d(\mathrm{LCL})/dt \gg 0$. (Along-band homogeneity of temperature and humidity contributes to weaker mixing within the modeled mesoscale updraft.) A combination of weak mixing and a high initial value of p^* might be marginally sufficient to achieve water saturation but insufficient to achieve the LFC before the parcel detrains from the mesoscale updraft, limiting cumulus to the forced stage.

The mesoscale updraft soundings (Fig. 18) indicate the action of persistent, localized moisture convergence and mesoscale lifting to produce a water-saturated cloud layer (and to reduce CIN to zero) from which deep moist convection subsequently grows. The process of destabilizing the CBL by persistent mesoscale lifting has previously been discussed by Crook and Moncrieff (1988). An interesting characteristic of the Crook and Moncrieff updraft sounding (illustrated by their Fig. 9) and our dryline soundings is the absolutely, convectively unstable stratification of the saturated layer. These unstably stratified saturated layers appear to represent a transient state that arises from the lifting (and nearly simultaneous saturation) of air parcels with differing p^* values in the vertically sheared westerly flow rather than the pure vertical displacement of air with a solitary source location and p^* value. The combination of an initially high moisture content and weak mixing during lifting may be sufficient to initiate deep convection, as illustrated by the cross sections (Figs. 7c, 11c, and 15c) and the mesoscale updraft soundings. If the mesoscale updraft is not sufficiently strong at cloud base, intense deep convection is not likely since growing cumulus towers require large vertical mass fluxes at cloud base to avoid dynamically entraining dry air through the sides of the cloud.

c. The impact of convective instability on convective initiation

We have analyzed atmospheric stability parameters from selected NSSL M-CLASS and model output soundings, displayed in Figs. 8, 12, 16, and 18, as well as from the model output fields. The M-CLASS soundings have been obtained within about 40 km of the dryline on all days, and potential horizontal inhomogeneities are neglected in comparing the observed and modeled soundings. Layer-averaged parcels in the simulated dryline environment are about 1.5 K potentially warmer and 0.5 g kg^{-1} drier than observed (i.e., ''nssl2'' versus ''model'' in Table 4). Observed and modeled values of CAPE are comparable on all days. Simulated conditions at the mesoscale updraft along the dryline (i.e., ''conv'' in Table 4) are significantly warmer and more moist and accordingly (despite some latent heating of the column below the LFC in the dryline cases) have much larger CAPE values than in the modeled near-dryline environment, illustrating the increase of layer-averaged parcel instability from moisture convergence (Pielke and Zeng 1989).

Lifting of saturated air parcels above their LFC is required to initiate deep convection. Moisture convergence along the mesoscale updraft bands destabilizes the local sounding to deep convection, while simultaneously decreasing the CIN to zero where storms subsequently develop. Simulated convective clouds of all modes, including shallow forced cumulus and storms, develop in regions where the CIN ranges from zero up to the order of the peak kinetic energy of the boundary layer updraft, or equivalently where $w_{\max} \geq (2\ \mathrm{CIN})^{0.5}$ (i.e., ''WCIN'' in Table 4), and moisture is sufficiently deep to permit water saturation to develop in the boundary layer (Figs. 7b,c; 11b,c; and 15b,c). Conversely, the broad regions of subsidence between the mesoscale updraft bands suppress cloud development and increase CIN. Regardless of whether the lifted parcel is an average of the lowest 75 mb of the boundary layer or originates at the level of minimum θ_v, the CIN values approach zero along the convergence lines where convection develops and are of order 10 J kg^{-1} or 100 J

TABLE 4. Sounding parameters related to convective initiation for the dryline study. The terms TBAR and QBAR are the average values of potential temperature (K) and vapor mixing ratio (g kg^{-1}) in the lowest 75 mb of the sounding, while the terms CIN, WCIN, and CAPE are defined in the text. The label ''nssl2'' denotes the mobile CLASS sounding near the dryline (C or X in Fig. 2), the label ''model'' denotes the model sounding near the dryline (M or X in Fig. 2), and the label ''conv'' denotes the model sounding within the dryline convergence band (U in Fig. 2). An asterisk indicates that the sounding did not attain the equilibrium level.

	15 May			16 May			26 May		
	nssl2	model	conv	nssl2	model	conv	nssl2	model	conv
TBAR	308.7	310.3	311.5	305.3	307.0	307.9	312.6	313.7	314.6
QBAR	8.3	8.3	11.9	8.7	7.6	13.5	11.7	11.3	12.4
CIN	45	15	0.5	164	147	0.3	57	17	0.5
	(67)	(82)	(0.4)	(151)	(157)	(1.2)	(73)	(41)	(3.1)
WCIN	10	6	1.0	18	17	0.8	11	6	1.0
	(12)	(13)	(0.9)	(17)	(18)	(1.6)	(12)	(9)	(2.5)
CAPE	749	1099	3244	158	221	3073	2013*	2230	3258

kg^{-1}, respectively, over the adjacent regions of downward motion. Lifting the minimum θ_v parcel is preferable to lifting the lowest 75-mb average parcel, or alternatively to lifting the surface parcel (e.g., Rennó and Williams 1995), in the sense that it most clearly distinguishes in the model results where dryline convection is imminent or has developed from areas that do not experience deep convective initiation.

Graziano and Carlson (1987) have proposed a lid strength index (LSI) to gauge the degree of inhibition to convection and have correlated LSI values from synoptic-scale NWS soundings to storm occurrence for a large group of storm events from a single warm season. The LSI is defined as the quantity $\theta_{swl} - \Theta_w$, where θ_{swl} is the saturation wet bulb potential temperature at the warmest level of the inversion capping the boundary layer and Θ_w is the average boundary layer wet bulb potential temperature. (The LSI is closely related to the maximum layer contribution to the vertical integral defining the CIN.) They find that deep convection is predictable if the lifted index LI < 0 and LSI ≤ 2, and that the likelihood of deep convection increases with decreasing values of the LI and LSI. Although a lid is often present and the LSI > 0, they report many other cases where the lid is absent and the LSI ≤ 0. Using much smaller horizontal spacing of soundings, we confirm the conclusions of Graziano and Carlson concerning the absence of a lid near deep convection and the decreasing probability of convection with increasing lid strength.

Colby (1984) suggests that convection is initiated when inhibition becomes small enough to allow turbulent and mesoscale vertical motions in the boundary layer to overcome the residual stability and lift air parcels to the LFC. Estimating the minimum value of CIN for the case studied as about 16 J kg^{-1} using a one-dimensional boundary layer model, Colby points out that a parcel vertical velocity of about 6 m s^{-1} would be required to overcome this residual stability and initiate convection. He suggests that such strong vertical motions are rarely achieved in the boundary layer and proposes that continued afternoon heating would be required to reduce the lid strength even further.

Rhea (1966) finds that ''no existing stable layer was found to be suppressing thunderstorm development in the unmixed moist air in the first 50 mi to the east of the estimated surface dry line location, yet thunderstorm development was much more frequent very near the dry line.'' Rhea speculates that ''even a slight organizing wind contrast zone will greatly increase the thunderstorm development frequency.'' Our sounding analysis (Table 4) and comparison of CIN and vertical motion fields (Figs. 7b, 11b, and 15b) confirm and extend the findings of the Colby and Rhea studies by suggesting that the joint occurrence of vanishingly small CIN values and vertical motions in the 1–5 m s^{-1} range are necessary (though not sufficient) conditions for convection to occur. In concert with the joint attainment of the vertical motion and CIN thresholds, *convective initiation requires an adequate moisture supply and limited parcel-relative increases of p* from mixing to meet the condition p* > p somewhere along an air trajectory passing through the mesoscale updraft band.* Our model results suggest that the banded moisture structures along simulated drylines promote conservation of *p** following the air motion owing to the introduction of a degree of horizontal homogeneity.

d. Morphology of simulated dryline convection

Mesoscale lift initially forces cumulus to develop along the updraft bands where that lift is sufficiently deep and moisture levels are adequate. Conditions for development of simulated deep convection are particularly favorable at or within a few tens of kilometers east of the dryline location. That the simulated convection develops in close proximity to the dryline is consistent with the observational findings of Rhea (1966) and Bluestein and Parker (1993). Modeling studies by Cotton et al. (1976) and Tao and Simpson (1984) have demonstrated the influence of boundary layer convergence on the morphology and organization of moist con-

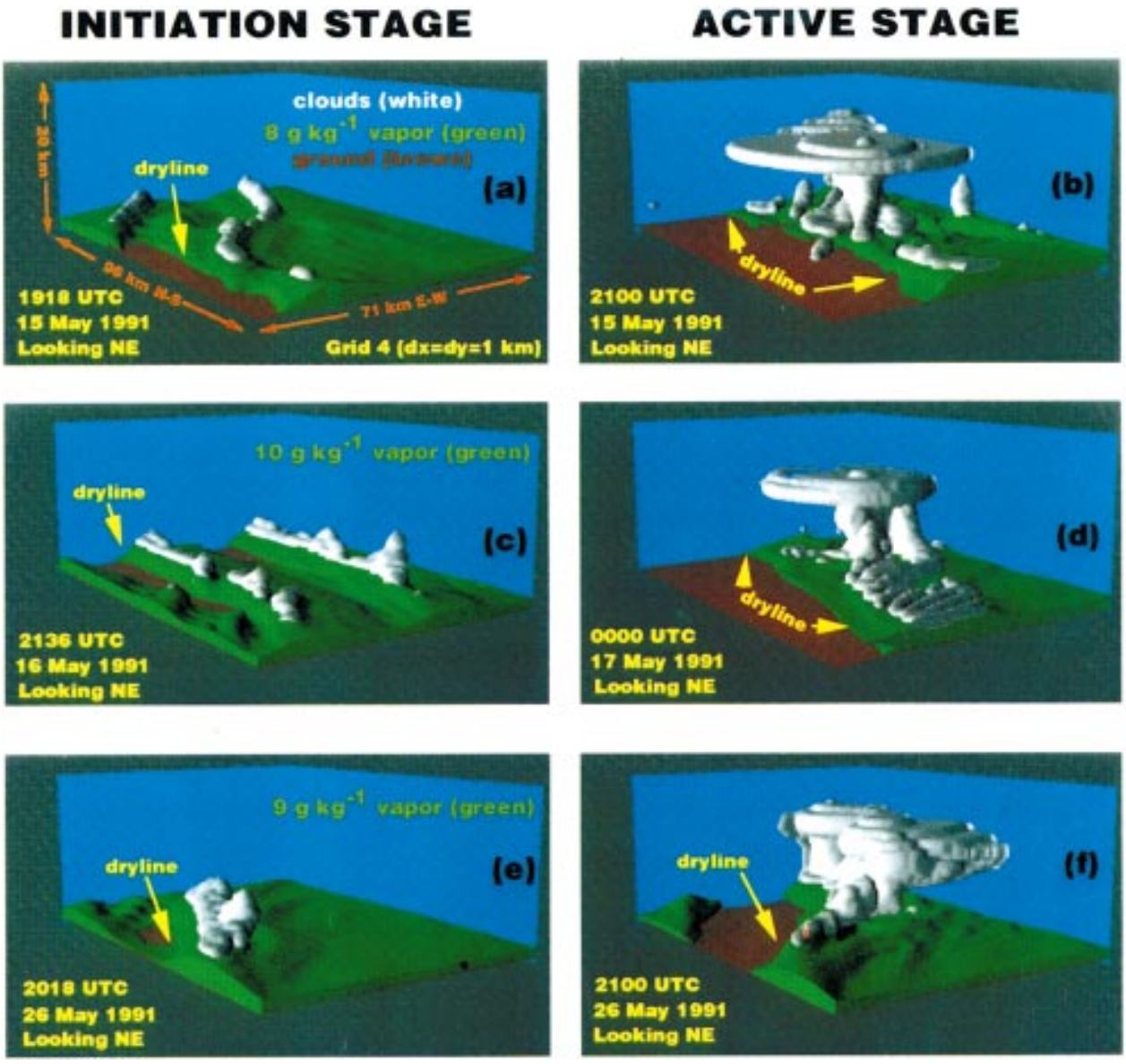

FIG. 19. Surfaces of cloud and constant vapor mixing ratios in perspective view on grid 4 at the initiation and active stages of simulated deep dryline convection. (a) 1918 UTC 15 May 1991; (b) 2100 UTC 15 May 1991; (c) 2136 UTC 16 May 1991; (d) 0000 UTC 17 May 1991; (e) 2018 UTC 26 May 1991; (f) 2100 UTC 26 May 1991. In panels (a) and (b), (c) and (d), and (e) and (f) the vapor mixing ratio surfaces have values of 8, 10, and 9 g kg^{-1}, respectively.

vection. One or more bands or patches of shallow or swelling cumulus develop in the model along significant updraft bands (Figs. 19a,c,e). Due to the variation of the LCL across the convergence band (discussed in section 4b), the forced cumulus clouds that initially develop have higher cloud bases on the dry side than on the moist side of the band. Due to the strong vertical wind shear across the convergence bands, the cloud bands slope toward the east as also noted for isolated dryline convection by McCaul and Blanchard (1990). In isolated locations along the updraft bands, sufficient latent heat release occurs to activate the cumulus due to the steep lapse rates of virtual temperature above the boundary layer (Figs. 7d, 11d, and 15d). As buoyant energy is realized, the model develops towering cumuli and some subsequently grow into deep convective storms (Figs. 19b,d,f).

The morphology and location of explicitly simulated convection relative to the dryline is broadly consistent with observed convection in visual satellite images. Satellite imagery in these and many other dryline cases reveal cumulus cloud bands that develop on the upwind flanks of deep convection, suggesting that the cloud development process is intimately connected to con-

vergence along these feeder bands. The cloud bands noted in satellite imagery and the model results reveal a progression from small cumulus and towering cumulus on the southwest, or upshear, end of the bands to deep convection on the northeast end of the bands. As a result of deep tropospheric wind shear effects and the development of precipitation-induced cold outflow boundaries, convection initially moves along a convergence band and ultimately propagates away from the northeastern end of the quasi-stationary genesis region. Individual cumuli move downshear along an updraft band, thereby maintaining the moisture flux supply at cloud base that is needed to sustain growth. Multiple rounds of deep dryline convection may develop from one or more cloud bands during the course of a simulation.

In the 15 May case, a cloud band begins forming along the dryline around 1900 in both the model and satellite imagery. Simulated deep convection develops by 2000 and is fully developed by midafternoon (Figs. 5b and 19b). In the 16 May case, cloud bands form around 2130 in the model and satellite imagery. By 0000 a large storm has developed from boundary layer cloud bands over northeast Oklahoma in the satellite imagery (Fig. 9b), the radar observations (Fig. 17), and the model (Fig. 19d). In the 26 May case, a cloud band develops along the dryline around 2000 in the model (Fig. 15b) and satellite imagery, evolving into a very strong storm after 2100 in the model (Fig. 19f). By 2300 this storm complex evolves into a large severe storm in northwestern Oklahoma (Fig. 13b). In the 15, 16, and 26 May cases, the model produces flanking line convective bands that are broadly similar to those features detected in the satellite imagery.

Our model results contain both forced and weakly active cumulus that do not grow into deep convection. The most prominent examples of forced cumulus are the shallow cloud bands along the dryline in the 15 May, 16 May, and 26 May cases. The animation of model output, with individual frames depicted as in Fig. 19, reveals localized undulations of the moist layer moving at a different phase velocity than the propagation velocity of the growing cumulus. Because the boundary layer perturbations move relative to the clouds, the boundary layer forcing is transient in a cloud-relative reference frame (e.g., Balaji and Clark 1988). In other cases, as for small, high-based clouds west of the dryline, the moisture supply and CAPE are limited and further diluted as the growing cumulus begins to entrain drier air from around cloud base within the inversion layer. In each case where deep convection did not develop, either very dry boundary layer air or the lack of an intense, deep, quasi-stationary boundary layer updraft band, or both factors, prevented cumulus from growing into deep convection.

In other work closely related to the present study, a series of sensitivity tests have been performed for the 15–16 May dryline case to explore the impact on mesoscale weather from the variation of soil moisture and vegetation cover (Shaw 1995; Pielke et al. 1997). The magnitudes of the eastward increase of soil moisture and/or leaf area index has a strong impact on the east–west heat flux gradient, perturbing the mesoscale boundary layer circulations and modifying the convective initiation process. Both the timing and mode of the simulated deep convection are sensitive to the assumed vegetation coverage (Pielke et al. 1997). A higher-LAI surface over western Oklahoma in the USGS vegetation run produces more vigorous surface layer heat fluxes and a deeper CBL east of the simulated dryline than in the low-LAI short grass run, while simultaneously producing stronger lifting from the thermally induced secondary circulations in the boundary layer. The deeper CBL in the USGS vegetation run makes the stronger mesoscale updrafts more effective at initiating convection by providing deeper moisture to support the development of water-saturated updrafts.

e. Implications for initializing classical dynamic cloud model simulations

It is of interest to contrast the methods used to initiate multidimensional dynamic cloud models with the present approach of full mesoscale simulation. Deep convection has typically been initiated in the classic cloud-scale simulations by generating localized lift from ''buoyant bubble'' perturbations of either potential temperature or absolute humidity, or both, that are superimposed on the horizontally homogeneous base-state initial conditions (e.g., Klemp and Wilhelmson 1978). Exceptions are studies by Dudhia and Moncrieff (1989) and Tao et al. (1991), in which a low-level cold pool was initialized to solenoidally force a secondary circulation in the boundary layer, and the study by Hane (1975), in which horizontal, diffuse, dryline-like moisture and temperature gradients and a vertical boundary layer circulation were specified. A hybrid approach was employed by Chang and Orville (1973), Tripoli and Cotton (1980), and Schlesinger (1988), who assumed horizontally homogeneous initial profiles and in some cases thermal bubbles, while simultaneously imposing a uniform weak mesoscale lift within the cloud initiation region. Uncertainty concerning the appropriate physical dimensions and amplitudes of the imposed thermal bubbles effectively restricts predictability of the convection thus initiated (McPherson 1992); similar ambiguity arises from imposing lift not derived from known or simulated mesoscale forcing.

The present findings suggest that a combination of thermal (i.e., both potential temperature and water vapor) and momentum perturbations are more appropriate approximations for initiating deep convection in dryline environments. It has been demonstrated that the focused mesoscale lift locally destabilizes the boundary layer to deep moist convection as CIN is reduced to zero. The initial perturbation of the simulated dryline convection is similar to a plume, with its kinetic energy being main-

tained from the external solenoid field and the unstable thermal stratification near the surface. Conversely, a thermal bubble has a finite buoyant energy content and rapidly deforms its buoyancy field due to transport by the intensifying toroidal circulation around the bubble's central vertical axis. Crook and Moncrief (1988) have concluded that convection generated by large-scale convergence could be quite distinct from convection generated by thermal bubbles. Hence, the plumes that initiate deep convection along the simulated drylines cannot be approximated by assuming a bubblelike initial thermal perturbation. Thus, predictability of the initial dryline convection is seen to depend on the joint evolution of the dynamically interrelated perturbations of moisture, mass, and momentum in the boundary layer.

It is intriguing that there appears to be considerable similarity between the type of sounding often used to initialize classic convective storm simulations (e.g., Klemp and Wilhelmson 1978) and the model soundings in the immediate vicinity of the drylines simulated in the present study. These ''proximity'' soundings in the present simulations (Fig. 18) feature almost homogeneously well-mixed profiles of potential temperature and vapor mixing ratio in the boundary layer, very small or zero values of CIN, and steep temperature lapse rates in the lower and middle troposphere. Our results suggest that such favorable conditions are achieved only within a narrow, roughly 10-km-wide zone along the dryline and that conditions only a few tens of kilometers to the east of the dryline are very different (e.g., Figs. 8, 12, and 16, and Table 4). Our simulated storms initially move along dryline segments oriented with the boundary layer wind shear, and soon thereafter propagate to the east of the dryline. Hence, cloud models assuming horizontally homogeneous initial conditions perturbed by the aforementioned thermal bubbles may not adequately simulate the evolution of dryline storms as they propagate away from their genesis regions.

f. Implications for operational mesoscale prediction of dryline convection

The Environmental Modeling Center (EMC) has recently developed and implemented an operational mesoscale version of the hydrostatic, step-mountain, eta coordinate model, with a 29-km horizontal grid spacing and 50 levels to provide enhanced vertical resolution in the boundary layer (Black 1994). It is anticipated that the ''meso-Eta'' model will undergo continual refinement of spatial resolution over the next 5–10 years (McPherson 1994), and a nonhydrostatic version of the mesoeta model is being developed (Gallus and Rančić 1996). A goal of this effort is to operationally implement the nonhydrostatic model on a fine mesh at approximately a 5-km grid spacing. Using a one-way nesting scheme, time-dependent variables from the hydrostatic mesoeta model could be continuously input to the nested nonhydrostatic model. Hence, the nested fine mesh of the nonhydrostatic EMC mesoscale model would provide spatial resolution comparable to that of the 5-km nested grid in the present study. These similarities of model physics and nested grid resolution permit speculation concerning potential issues and problems to be encountered in numerically forecasting the evolution of the dryline and the initiation of deep, moist dryline convection with the nonhydrostatic EMC mesoscale model.

Our model calculations validate the argument advanced by Ziegler et al. (1995) that grid meshes with grid spacings greater than about 20 km are too coarse to resolve the dryline itself. In addition to smoothing the moisture and temperature gradients, convergence and vertical motions so critical to cloud initiation are also not resolved. However, it is important to reiterate that the enhanced moisture gradient marking the approximate dryline location is clearly resolved on the grids with spacings greater than 20 km, a result consistent with many previous mesoscale modeling studies (Anthes et al. 1982; Kaplan et al. 1984; Koch 1985; Benjamin 1986; Benjamin and Carlson 1986; Lanicci et al. 1987; Lakhtakia and Warner 1987; Zack and Kaplan 1987; Chang and Wetzel 1991; Sun and Wu 1992; Kaplan and Karyampudi 1992). Since the CSU model appears to have some capability to accurately position the dryline on spatial scales of 50 km or less (i.e., several counties in width) at timescales of 6–12 h, it is reasonable to speculate that watch boxes enclosing areas of initial convection might ultimately be refined toward similar space and timescales using operational model output.

It must be emphasized that we have only demonstrated that successful research model simulations of drylines, and perhaps also of dryline convection, are possible. Considering the challenges of generating consistently accurate mesoscale numerical weather forecasts and providing end users with meaningful forecast products (Brooks et al. 1992), a demonstrated simulation capability is only a modest first step toward the arduous task of achieving *operational* numerical weather prediction of drylines and dryline convection. Although predictability should be limited by uncertainty of the joint profiles of temperature, humidity, and vertical air motion, the predicted moisture convergence fields may be broadly useful for anticipating the initiation of storms (Crook 1996). If verification studies of the EMC mesoscale model subsequently demonstrate that the dryline location can be reliably estimated for operational purposes, the use of EMC mesoscale model output could assist forecasters in preparing refined forecasts of, at minimum, the initial east–west location of drylines and the potential for and timing of dryline convection.

With nonhydrostatic flow dynamics in the presence of convective instability and mesoscale vertical motion to serve as a ''trigger,'' simulated deep convective clouds develop along the dryline on the 5-km mesh. The two darkly shaded areas in Fig. 6a illustrate the moisture

convergence field and dimensions of the cloud bases of typical deep convection on the 5-km grid in the 15 May case (Fig. 6b). The main updrafts of the convection on the 5-km mesh are 10–15 km in width, while the peak updrafts are only about 10 m s^{-1} in magnitude. Although the internal dynamical and microphysical processes in this ''pseudo-convection'' are as in real convection, the 5-km grid spacing does not properly resolve even basic attributes such as updraft width and intensity. Under the assumption that the nested version of the mesoeta model would in effect have the same dynamical framework as the CSU-RAMS, we speculate that there could be some occurrences of ''pseudo-convection'' in mesoeta forecasts of dryline environments with convective potential. Despite these uncertainties, pseudo-dryline convection develops within a few tens of kilometers and 1 h of observed convection. Hence, the occurrence of pseudo-convection in EMC mesoscale model forecasts might have limited usefulness in refining the initial location and timing of regional convective outbreaks along the dryline.

5. Conclusions

This paper reports the results of simulations of moist convection along drylines developing on the southern U.S. plains during May of 1991. A nonhydrostatic, three-dimensional version of the CSU-RAMS is used to deduce the processes responsible for initiating and maintaining dryline convection. Both the formation of drylines and the subsequent initiation of deep dryline convection have been explicitly simulated in the 15, 16, and 26 May cases, and deep moist convection is observed along these drylines. The mesoscale model simulates various types of convection, including shallow, forced isolated cumuli and cumulus bands as well as active deep convection including towering cumuli and cumulonimbi with anvils (i.e., storms). Simulated deep convection often develops explosively at the downwind end of a cloud band, suggesting a feeder process.

In the simulations, narrow convergence bands in the CBL provide the lift to initiate deep moist dryline convection. The thermally direct secondary dryline circulations are frontogenetic and primarily solenoidally forced. Maximum updrafts reach 5 m s^{-1} and the bands are 3–9 km wide and 10–100 km in length. The updrafts penetrate and are decelerated or restricted by the overlying stable air above the CBL, reaching depths of about 2000 m in the cases studied. The dryline is collocated with a moisture convergence band and ''multiple drylines'' may be simulated. The wavelike character of the simulated drylines and their moisture convergence bands are suggestive of mesoscale dryline waves (MDLWs) reported in previous studies.

Other simulated convergence bands develop on either side of the dryline in convectively unstable boundary layers characterized by moderate speed and directional wind shear. These convergence bands are, as the simulated drylines, manifestations of horizontal boundary layer roll vortices. In such environments linear theory of inflection-point or convective instability predicts development of classical horizontal convective rolls (HCRs) with ''aspect ratios'' of 2–4. Hence, the simulated roll-like circulations (with aspect ratios in the range of 7–23) cannot be explained by linear theory. Fine line radar echoes observed in the CBL in the 16 May case have spacings consistent with the simulated convergence bands on either side of the dryline, suggesting a possible connection to ''large aspect ratio'' roll vortices that have been reported in the literature.

The mesoscale updraft bands provide the lifting needed to elevate moist air from the lower CBL to the LCL, initiating forced cumulus, and ultimately to the LFC, initiating active deep convection. Model soundings in the mesoscale updrafts reveal rather small lapse rates of potential temperature and vapor mixing ratio where clouds form, suggesting that increases of the LCL and LFC due to mixing following the parcel motion are also small. Stability analysis of the model soundings indicates a preference of convective initiation where moisture convergence in the mesoscale updraft has locally reduced CIN to zero. Conversely, relatively large vapor mixing ratio lapse rates away from the mesoscale updrafts are indicative of the downward entrainment of dry air into the CBL from above. This implies that parcel theory, which assumes that the Saturation Point is fixed following the motion, is approximately satisfied only within the mesoscale updrafts and is violated elsewhere in the prestorm CBL. Though CIN increases rather slowly away from the mesoscale updrafts in the direction of increasing moisture and CAPE, deep convective initiation occurs only along the mesoscale updrafts. The combination of deep mesoscale lift (with vanishing CIN), weak mixing following the motion, and high boundary layer humidities appear to be necessary for deep convection to form.

Our findings suggest that classical cloud models may not adequately simulate the early development of dryline storms. While storms are usually initiated in classical models with buoyant bubbles placed in a horizontally homogeneous, stably or neutrally stratified sheared environment, both our mesoscale simulations and previous observational studies indicate that the dryline environment has strong horizontal inhomogeneities of moisture, convective instability, and shear. We have also documented that the mesoscale updraft band responsible for cloud initiation behaves more like a quasi-steady, roll-like, weakly buoyant plume than a highly transient thermal bubble.

Our results suggest that cautious optimism may be warranted in regard to operational numerical prediction of drylines and the threat of attendant deep convection. Predictability of the relevant modeled boundary layer phenomena is likely to be restricted by the inhomogeneous structure of the dryline environment and sensitivity of the model simulation or forecast to such factors

as the vegetation model and its key parameters, the soil moisture analysis, the initial and boundary conditions employed, and the numerical grid configuration and resolution. Simulated deep convection is poorly resolved on coarse grids with spacings around 5 km and may be very sensitive to uncertainties regarding the initial environmental state, which in turn could arise from measurement errors or a lack of mesoscale observations of sufficient density. In addition, no operationally tested subgrid convective parameterization scheme exists for grids with spacings less than 20 km. In view of these limitations, we interpret our model results as providing guidance regarding dryline evolution and the possible convective initiation mechanisms that occur along drylines in nature. These complete and internally consistent output data sets could be used to aid in designing sampling strategies for possible future field studies of the convective initiation process.

Acknowledgments. The initial model fields for the simulations were generated on the National Center for Atmospheric Research (NCAR) Cray-YMP (Shavano) under Grant ATM 8915265 to Colorado State University, while the numerical simulations were performed on an IBM RS-6000 workstation at the NSSL. Robert Walko, Peter Olsson, Jeff Copeland, and Brent Shaw (all formerly or currently affiliated with CSU) are gratefully acknowledged for assisting in the installation of the CSU model on the computers. The PAM mesonetwork was operated by NCAR-Atmospheric Technology Division (ATD) during COPS-91. We gratefully acknowledge the assistance of Robert Rilling (NCAR-ATD) to help us access the PAM data from the 1991 program. Lou Steyaert (USGS) provided professional input and access to land use data (USGS Grant 1434-94-A-1275 to CSU). An earlier version of the manuscript was improved by comments offered by Jeanne Schneider and Dave Stensrud; thoughtful formal reviews by Andrew Crook and an anonymous referee are also gratefully acknowledged. NCAR is sponsored by the National Science Foundation. The NLDN is operated by Global Atmospherics, Inc., of Tuscon, Arizona.

REFERENCES

Anthes, R. A., Y.-H. Kuo, S. G. Benjamin, and Y.-F. Li, 1982: The evolution of the mesoscale environment of severe local storms: Preliminary modeling results. *Mon. Wea. Rev.*, **110,** 1187–1213.

Atkins, N. T., R. M. Wakimoto, and T. M. Weckwerth, 1995: Observations of the sea-breeze front during CaPE. Part II: Dual-Doppler and aircraft analysis. *Mon. Wea. Rev.*, **123,** 944–969.

Avissar, R., and Y. Mahrer, 1988: Mapping frost-sensitive areas with a three-dimensional local-scale numerical model. Part I: Physical and numerical aspects. *J. Appl. Meteor.,* **27,** 400–413.

Balaji, V., and T. L. Clark, 1988: Scale selection in locally forced convective fields and the initiation of deep cumulus. *J. Atmos. Sci.,* **45,** 3188–3211.

Banta, R. M., 1984: Daytime boundary-layer evolution over mountainous terrain. Part I: Observations of the dry circulations. *Mon. Wea. Rev.,* **112,** 340–356.

——, and C. B. Schaaf, 1987: Thunderstorm genesis zones in the Colorado Rocky Mountains as determined by traceback of geosynchronous satellite images. *Mon. Wea. Rev.,* **115,** 463–476.

Battan, L. J., 1965: Some factors governing precipitation and lightning from convective clouds. *J. Atmos. Sci.,* **22,** 79–84.

Benjamin, S. G., 1986: Some effects of surface heating and topography on the regional severe storm environment. *Mon. Wea. Rev.,* **114,** 307–343.

——, and T. N. Carlson, 1986: Some effects of surface heating and topography on the regional severe storm environment. Part I: 3D simulations. *Mon. Wea. Rev.,* **114,** 330–343.

Betts, A. K., and J. H. Ball, 1995: The FIFE surface diurnal cycle climate. *J. Geophys. Res.,* **100,** 25 679–25 693.

Black, T. L., 1994: The new NMC mesoscale eta model: Description and forecast examples. *Wea. Forecasting,* **9,** 265–278.

Bluestein, H. B., 1994: High-based funnel clouds in the southern Plains. *Mon. Wea. Rev.,* **122,** 2631–2638.

——, and S. S. Parker, 1993: Modes of isolated, severe convective storm formation along the dryline. *Mon. Wea. Rev.,* **121,** 1352–1374.

Brooks, H. E., C. A. Doswell III, and R. A. Maddox, 1992: On the use of mesoscale and cloud-scale models in operational forecasting. *Wea. Forecasting,* **7,** 120–132.

Brown, R. A., 1980: Longitudinal instabilities and secondary flows in the planetary boundary layer: A review. *Rev. Geophys. Space Phys.,* **18,** 683–697.

Carbone, R. E., J. W. Conway, N. A. Crook, and M. W. Moncrieff, 1990: The generation and propagation of a nocturnal squall line. Part I: Observations and implications for mesoscale predictability. *Mon. Wea. Rev.,* **118,** 26–49.

Carlson, T. N., and F. H. Ludlam, 1968: Conditions for the formation of severe local storms. *Tellus,* **20,** 203–226.

——, S. G. Benjamin, G. S. Forbes, and Y.-F. Li, 1983: Elevated mixed layers in the severe-storm environment: Conceptual model and case studies. *Mon. Wea. Rev.,* **111,** 1453–1473.

Chang, J.-T., and P. J. Wetzel, 1991: Effects of spatial variation of soil moisture and vegetation on the evolution of a prestorm environment: A numerical case study. *Mon. Wea. Rev.,* **119,** 1368–1390.

Chang, S. W., and H. D. Orville, 1973: Large-scale convergence in a numerical cloud model. *J. Atmos. Sci.,* **30,** 947–950.

Clark, C. A., and R. W. Arritt, 1995: Numerical simulations of the effect of soil moisture and vegetation cover on the development of deep convection. *J. Appl. Meteor.,* **34,** 2029–2045.

Colby, F. P., 1984: Convective inhibition as a predictor of convection during AVE-SESAME II. *Mon. Wea. Rev.,* **112,** 2239–2252.

Cotton, W. R., and R. A. Anthes, 1989: *Storm and Cloud Dynamics.* Academic Press, 883 pp.

——, R. A. Pielke, and P. T. Gannon, 1976: Numerical experiments on the influence of the mesoscale circulations on the cumulus scale. *J. Atmos. Sci.,* **33,** 252–261.

Crook, N. A., 1996: Sensitivity of moist convection forced by boundary layer processes to low-level thermodynamic fields. *Mon. Wea. Rev.,* **124,** 1767–1785.

——, and M. W. Moncrieff, 1988: The effect of large-scale convergence on the generation and maintenance of deep moist convection. *J. Atmos. Sci.,* **45,** 3606–3624.

Dickinson, R. E., A. Henderson-Sellers, P. Kennedy, and M. Wilson, 1986: Biosphere–Atmosphere Transfer Scheme (BATS) for the NCAR Community Climate Model. NCAR/TN-275+STR, 81 pp. [NTIS #PB87-141511.]

Doswell, C. A., III, 1982: The operational meteorology of convective weather. Vol. I: Operational mesoanalysis. NOAA Tech. Memo. NWS NSSFC-5, 164 pp. [NTIS # PB83162321.]

——, 1987: The distinction between large-scale and mesoscale contribution to severe convection: A case study example. *Wea. Forecasting,* **2,** 3–16.

——, and E. N. Rasmussen, 1994: The effect of neglecting the virtual temperature correction on CAPE calculations. *Wea. Forecasting,* **9,** 625–629.

Dudhia, J., and M. W. Moncrieff, 1989: A three-dimensional numerical study of an Oklahoma squall line containing right flank supercells. *J. Atmos. Sci.,* **46,** 3363–3391.

Etling, D., and R. A. Brown, 1993: Roll vortices in the planetary boundary layer: A review. *Bound.-Layer Meteor.,* **65,** 215–248.

Fankhauser, J. C., N. A. Crook, J. Tuttle, L. J. Miller, and C. G. Wade, 1995: Initiation of deep convection along boundary layer convergence lines in a semitropical environment. *Mon. Wea. Rev.*, **123,** 291–313.

Gallus, W. A., Jr., and M. Rančić, 1996: A non-hydrostatic version of the NMC's regional Eta model. *Quart. J. Roy. Meteor. Soc.*, **122,** 495–513.

Grasso, L. D., 1996: Numerical simulation of the May 15 and April 26, 1991 thunderstorms. Colorado State University Dept. of Atmospheric Sciences Paper 596, 151 pp. [Available from Colorado State University, Dept. of Atmospheric Sciences, Foothills Campus, Ft. Collins, CO 80523.]

Graziano, T. M., and T. N. Carlson, 1987: A statistical evaluation of lid strength on deep convection. *Wea. Forecasting,* **2,** 127–139.

Hane, C. E., 1975: The trajectories of dropsondes in simulated thunderstorm circulations. *Mon. Wea. Rev.,* **103,** 709–716.

——, C. L. Ziegler, and H. B. Bluestein, 1993: Investigation of the dryline and convective storms initiated along the dryline: Field experiments during COPS-91. *Bull. Amer. Meteor. Soc.,* **74,** 2133–2145.

Johns, R. H., and C. A. Doswell III, 1992: Severe local storms forecasting. *Wea. Forecasting,* **7,** 588–612.

Kaplan, M. L., and V. M. Karyampudi, 1992: Meso-beta scale numerical simulations of terrain drag-induced along-stream circulations. Part II: Concentration of potential vorticity within dryline bulges. *Meteor. Atmos. Phys.,* **49,** 157–185.

——, J. W. Zack, V. C. Wong, and G. D. Coats, 1984: The interactive role of subsynoptic scale jet streak and planetary boundary layer processes in organizing an isolated convective complex. *Mon. Wea. Rev.,* **112,** 2212–2237.

Karyampudi, V. M., S. E. Koch, C. Chen, J. W. Rottman, and M. D. Kaplan, 1995: The influence of the Rocky Mountains on the 13–14 April 1986 severe weather outbreak. Part II: Evolution of a prefrontal bore and its role in triggering a squall line. *Mon. Wea. Rev.,* **123,** 1423–1446.

Keyser, D., and T. N. Carlson, 1984: Transverse ageostrophic circulations associated with elevated mixed layers. *Mon. Wea. Rev.,* **112,** 2465–2478.

Klemp, J. B., and R. B. Wilhelmson, 1978: The simulation of three-dimensional convective storm dynamics. *J. Atmos. Sci.,* **35,** 1070–1096.

Koch, S. E., 1984: The role of an apparent mesoscale frontogenetic circulation in squall line initiation. *Mon. Wea. Rev.,* **112,** 2090–2111.

——, 1985: Ability of a regional-scale model to predict the genesis of intense mesoscale convective systems. *Mon. Wea. Rev.,* **113,** 1693–1713.

——, and J. McCarthy, 1982: The evolution of an Oklahoma dryline. Part II: Boundary-layer forcing of mesoconvective systems. *J. Atmos. Sci.,* **39,** 237–257.

Lakhtakia, M. N., and T. T. Warner, 1987: A real-data numerical study of the development of precipitation along the edge of an elevated mixed layer. *Mon. Wea. Rev.,* **115,** 156–168.

Lanicci, J. M., and T. T. Warner, 1991: A synoptic climatology of the elevated mixed-layer inversion over the southern Great Plains in spring. Part II: The life cycle of the lid. *Wea. Forecasting,* **6,** 198–213.

——, T. N. Carlson, and T. T. Warner, 1987: Sensitivity of the Great Plains severe-storm environment to soil-moisture distribution. *Mon. Wea. Rev.,* **115,** 2660–2673.

Lee, T. J., 1992: The impact of vegetation on the atmospheric boundary layer and convective storms. Colorado State University Dept. of Atmospheric Sciences Paper 509, 137 pp. [Available from Colorado State University, Dept. of Atmospheric Sciences, Foothills Campus, Ft. Collins, CO 80523.]

McCarthy, J., and S. E. Koch, 1982: The evolution of an Oklahoma dryline. Part I: A meso- and subsynoptic-scale analysis. *J. Atmos. Sci.,* **39,** 225–236.

McCaul, E. W., Jr., and D. O. Blanchard, 1990: A low-precipitation cumulonimbus along the dryline in Colorado. *Mon. Wea. Rev.,* **118,** 2768–2773.

McCumber, M. C., and R. A. Pielke, 1981: Simulation of the effects of surface fluxes of heat and moisture in a mesoscale numerical model. Part I: Soil layer. *J. Geophys. Res.,* **86,** 9929–9938.

McNulty, R. P., 1995: Severe and convective weather: A Central Region forecasting challenge. *Wea. Forecasting,* **10,** 187–202.

McPherson, R. A., 1992: Predictability experiments of a numerically-modeled supercell storm. CAPS Scientific Rep. 92-001, 128 pp. [Available from the Center for Analysis and Prediction of Storms, University of Oklahoma, Energy Center, 100 E. Boyd, Norman, OK 73109.]

McPherson, R. D., 1994: The National Centers for Environmental Prediction: Operational, climate, ocean, and weather prediction for the 21st century. *Bull. Amer. Meteor. Soc.,* **75,** 363–373.

Nicholls, M. E., R. A. Pielke, and W. R. Cotton, 1991: A two-dimensional numerical investigation of the interaction between sea breezes and deep convection over the Florida Peninsula. *Mon. Wea. Rev.,* **119,** 298–323.

NSSP Staff, 1963: Environmental and thunderstorm structures as shown by National Severe Storms Project observations in spring 1960 and 1961. *Mon. Wea. Rev.,* **91,** 271–292.

Ogura, Y., and Y. Chen, 1977: A life history of an intense mesoscale convective storm in Oklahoma. *J. Atmos. Sci.,* **34,** 1458–1476.

——, H. Juang, K. Zhang, and S. Soong, 1982: Possible triggering mechanisms for severe storms in SESAME-AVE IV (9–10 May 1979). *Bull. Amer. Meteor. Soc.,* **63,** 503–515.

Orlanski, I., 1975: A rational subdivision of scales for atmospheric processes. *Bull. Amer. Meteor. Soc.,* **56,** 527–530.

Parsons, D. B., M. A. Shapiro, R. M. Hardesty, R. J. Zamora, and J. M. Intrieri, 1991: The finescale structure of a west Texas dryline. *Mon. Wea. Rev.,* **119,** 1242–1258.

Pielke, R. A., 1984: *Mesoscale Meteorological Modeling.* Academic Press, 612 pp.

——, and X. Zeng, 1989: Influence on severe storm development of irrigated land. *Natl. Wea. Digest,* **14,** 16–17.

——, A. Song, P. J. Michaels, W. A. Lyons, and R. W. Arritt, 1991a: The predictability of sea-breeze generated thunderstorms. *Atmósphera,* **4,** 65–78.

——, G. A. Dalu, J. S. Snook, T. J. Lee, and T. G. F. Kittel, 1991b: Nonlinear influence of mesoscale land use on weather and climate. *J. Climate,* **4,** 1053–1069.

——, and Coauthors, 1992: A comprehensive meteorological modeling system—RAMS. *Meteor. Atmos. Phys.,* **49,** 69–91.

——, T. J. Lee, J. H. Copeland, J. L. Eastman, C. L. Ziegler, and C. A. Finley, 1997: Use of USGS-provided data to improve weather and climate simulations. *Ecol. Appl.,* in press.

Piepgrass, M. V., E. P. Krider, and C. B. Moore, 1982: Lightning and surface rainfall during Florida thunderstorms. *J. Geophys. Res.,* **87,** 11 193–11 201.

Rennó, N. O., and E. R. Williams, 1995: Quasi-Lagrangian measurements in convective boundary layer plumes and their implications for the calculation of CAPE. *Mon. Wea. Rev.,* **123,** 2733–2742.

Rhea, J. O., 1966: A study of thunderstorm formation along drylines. *J. Appl. Meteor.*, **5,** 58–63.

Rust, W. D., R. P. Davies-Jones, D. W. Burgess, R. A. Maddox, L. C. Showell, T. C. Marshall, and D. K. Lauritzen, 1990: Testing a mobile version of a Cross-chain LORAN Atmospheric Sounding System (M-CLASS). *Bull. Amer. Meteor. Soc.*, **71,** 173–180.

Schaaf, C. B., J. Wurman, and R. M. Banta, 1988: Thunderstorm-producing terrain features. *Bull. Amer. Meteor. Soc.,* **69,** 272–277.

Schaefer, J. T., 1986: The dryline. *Mesoscale Meteorology and Forecasting,* P. S. Ray, Ed., Amer. Meteor. Soc., 549–572.

Schlesinger, R. E., 1988: Effects of stratospheric lapse rate on thun-

derstorm cloud-top structure in a three-dimensional numerical simulation. Part I: Some basic results of comparative experiments. *J. Atmos. Sci.,* **45,** 1555–1570.

Segal, M., and R. W. Arritt, 1992: Nonclassical mesoscale circulations caused by surface sensible heat flux gradients. *Bull. Amer. Meteor. Soc.,* **73,** 1593–1604.

——, ——, C. Clark, R. Rabin, and J. Brown, 1995: Scaling evaluation of the effect of surface characteristics on potential for deep convection over uniform terrain. *Mon. Wea. Rev.,* **123,** 383–400.

Shaw, B. L., 1995: The effect of soil moisture and vegetation heterogeneity on a Great Plains dryline: A numerical study. Colorado State University Dept. of Atmospheric Sciences Paper 576, 93 pp. [Available from Colorado State University, Dept. of Atmospheric Sciences, Foothills Campus, Ft. Collins, CO 80523.]

Stull, R. B., 1985: A fair-weather cumulus cloud classification scheme for mixed-layer studies. *J. Climate Appl. Meteor.,* **24,** 49–56.

Sun, W.-Y., and Y. Ogura, 1979: Boundary layer forcing as a possible trigger to a squall line formation. *J. Atmos. Sci.,* **36,** 235–254.

——, and C.-C. Wu, 1992: Formation and diurnal variation of the dryline. *J. Atmos. Sci.,* **49,** 1606–1619.

Tao, W.-K., and J. Simpson, 1984: Cloud interactions and merging: Numerical simulations. *J. Atmos. Sci.,* **41,** 2901–2917.

——, ——, and S.-T. Soong, 1991: Numerical simulation of a subtropical squall line over the Taiwan Strait. *J. Atmos. Sci.,* **48,** 2699–2723.

Tripoli, G. J., and W. R. Cotton, 1980: A numerical investigation of several factors contributing to the observed variable intensity of deep convection over south Florida. *J. Appl. Meteor.,* **19,** 1037–1063.

U.S. Dept. of Agriculture (USDA), 1951: Soil survey manual. U.S. Dept. of Agriculture Publication 274, 503 pp. [Available from U.S. Dept. of Agriculture, Washington, DC 20009.]

U.S. Dept. of Commerce (USDOC), 1991: *Storm Data,* **33** (5), 260 pp.

——, and U.S. Dept. of Agriculture (USDOC/USDA), 1991a: *Weekly Weather and Crop Bulletin,* **78** (20), 24 pp.

——, and ——, 1991b: *Weekly Weather and Crop Bulletin,* **78** (22), 24 pp.

Wakimoto, R. M., and N. T. Atkins, 1994: Observations of the seabreeze front during CaPE. Part I: Single-Doppler, satellite, and cloud photogrammetry analysis. *Mon. Wea. Rev.,* **122,** 1092–1114.

Weston, K. J., 1972: The dry-line of northern India and its role in cumulonimbus convection. *Quart. J. Roy. Meteor. Soc.,* **98,** 519–531.

Wetzel, P. J., and J.-T. Chang, 1988: Evaporation from nonuniform surfaces: A first approach for short-term numerical weather prediction. *Mon. Wea. Rev.,* **116,** 600–621.

Wilson, J. W., J. A. Moore, G. B. Foote, B. Martner, A. R. Rodi, T. Uttal, and J. M. Wilczak, 1988: Convection initiation and downburst experiment (CINDE). *Bull. Amer. Meteor. Soc.,* **69,** 1328–1348.

——, T. M. Weckwerth, J. Vivekanandan, R. M. Wakimoto, and R. W. Russell, 1994: Boundary layer clear air radar echoes: Origin of echoes and accuracy of derived winds. *J. Atmos. Oceanic Technol.,* **11,** 1184–1206.

Zack, J. W., and M. L. Kaplan, 1987: Numerical simulations of the subsynoptic features associated with the AVE-SESAME I case. Part I: The preconvective environment. *Mon. Wea. Rev.,* **115,** 2367–2394.

Ziegler, C. L., and C. E. Hane, 1993: An observational study of the dryline. *Mon. Wea. Rev.,* **121,** 1134–1151.

——, P. S. Ray, and N. C. Knight, 1983: Hail growth in an Oklahoma multicell storm. *J. Atmos. Sci.,* **40,** 1768–1791.

——, W. J. Martin, R. A. Pielke, and R. L. Walko, 1995: A modeling study of the dryline. *J. Atmos. Sci.,* **52,** 263–285.